PARAMETRIC STUDY OF THREE-STRINGER-PANEL COMPRESSION-AFTER-IMPACT STRENGTH

Carl Q. Rousseau
J. Donn Hethcock
Bell Helicopter Textron, Inc.
Fort Worth, Texas 76101

Donald J. Baker
USA ARL/VTD
NASA Langley Research Center,
Hampton, VA 23681

Parametric Study of Three-Stringer-Panel Compression-After-Impact Strength

*Carl Q. Rousseau   †Donald J. Baker   ‡J. Donn Hethcock

AUTHOR'S AFFILIATION:

*Principal Engineer, Bell Helicopter Textron Inc., P.O. Box 482,

Fort Worth, TX 76101.

†Research Scientist, USA ARL/VTD, NASA Langley Research Center,

Hampton, VA 23681

‡Sr. Engineering Specialist, Bell Helicopter Textron Inc., P.O. Box 482,

Fort Worth, TX 76101

ABSTRACT:

Damage tolerance requirements for integrally-stiffened composite wing skins are typically met using design allowables generated by testing impact-damaged subcomponents, such as three-stringer stiffened panels. To improve these structures, it is necessary to evaluate the critical design parameters associated with three-stringer stiffened-panel compressive behavior. During recent research and development programs, four structural parameters were identified as sources for strength variation: (a) material system, (b) stringer configuration, (c) skin layup, and (d) form of axial reinforcement (tape versus pultruded carbon rods). Relative effects of these parameters on damage resistance and damage tolerance were evaluated numerically and experimentally. Material system and geometric configuration had the largest influence on damage resistance; location and extent of the damage zone influenced the sublaminate buckling behavior, failure initiation site, and compressive ultimate strength. A practical global-local modeling technique captured observed experimental behavior and has the potential to identify critical damage sites and estimate failure loads prior to testing. More careful consideration should be given to accurate simulation of boundary conditions in numerical and experimental studies.

KEYWORDS:

composite material, structure, damage tolerance, impact, compression, experimental, numerical, wing, stringer

Introduction

In the field of applied composite structural mechanics, a great deal of time and effort has been devoted to ensuring the structural integrity of aircraft components in the presence of low velocity impact damage. The low velocity impact threat has long been viewed as the most critical type of in-service damage for laminated composite structures[1]; thus all certifying/specifying agencies have explicit impact damage requirements as part of their more general static strength and/or damage tolerance rules [1–3]. Numerous publications have defined the general problem and offered both experimental and analytical studies of various critical variables [e.g., 4–10]. The purpose of this paper is to add to the current body of knowledge by collecting available compression-after-impact (CAI) data from a variety of sources and attempting to isolate and evaluate several key structural parameters. A brief description of damage resistance, damage tolerance, and the generic three-stringer panel problem will be given in the following introductory subsections, followed by a statement of the scope and objective of this parametric study.

Damage Resistance and Damage Tolerance

The framework for this study is set by regulatory static strength and damage tolerance requirements and accepted methods of quantifying damage and assessing its criticality. Specifically, such a regulation is the Federal Aviation Administration (FAA) Advisory Circular

---

[1] Discrete source damage (DSD) from ballistic or uncontained engine failure threats is another important damage tolerant design consideration. While DSD has sized large portions of composite structure in fixed-wing aircraft designs, CAI has proven to be the main design driver in Bell Helicopter military and civil tiltrotor aircraft.

AC29-2B, "Certification of Transport Category Rotorcraft," Section (g)(5), which requires that

"static strength substantiation should consider . . . impact damage expected during service up to

the established threshold of detectability of the field inspection methods to be employed." The

field inspection methods are assumed to be visual; thus the established threshold of detectability

is commonly defined as "barely visible impact damage" (BVID). BVID is quantified by

performing an impact survey on a representative structure and choosing a particular energy level

or dent depth, with concurrence of the regulatory or specifying agency. Usually an upper bound

energy level of 135 J (1200 in·lb) is used for thick structure, based on a U.S. Air Force study of

impact threats such as tool-drop (some form of through-penetration damage tolerance is required

for thin-gage structure).

Note that a structure's *resistance* to damage is not relevant to flight safety. Only the

tolerance of undiscovered/unrepaired damage under flight conditions is of concern to the

regulator. Nonetheless, for substantiation purposes, as well as for economic durability reasons,

the damage resistance of a structure must be separately characterized, at least to the extent of

identifying a threshold of detectability. This characterization effort typically takes the form of

the above-noted impact damage survey. This survey introduces the first of several parameters,

which affects the resulting level of damage tolerance. These parameters are the boundary

conditions (in terms of both panel support and location relative to geometric details such as the

stringers and ply edges) for the impact events and the energy and tip geometry of the indenter.

The damage tolerance of a structure is determined by imposing the worst-case impact

damage (the location on the structure where the BVID energy-level is highest) and testing to

failure under the most critical loading condition, usually compression. The resulting strength or

strain to failure is then reduced to account for environmental and statistical effects, and used as a

special design allowable over the whole expanse of primary structure represented by the tested configuration.

The Three-Stringer Panel Problem

In order to realistically simulate the boundary conditions of stiffened panel structures (both for the impact event and subsequent residual strength testing), the common approach is to provide one stringer and two adjacent skin bays for the test region, with a stringer on either side to approximate the proper widthwise and skin-bay constraint. The length of the specimen is determined by the maximum rib or frame spacing (assumed to be the worst case for compressive stability). Panels are often flat rather than curved, in order to simplify specimen fabrication. This simplification is generally assumed to be conservative (for curvature transverse to the loading direction), since it should yield lower results than would a curved panel. Another conservative simplification is in the form of end supports for the impact events. Specimen ends are typically clamped in wooden forms or potted in epoxy casting material (required for subsequent compression testing). Both of these end conditions are assumed to absorb less energy from the impact event than deeper, less stiff rib or frame webs, thus imparting more energy to the test panel than would be seen by the actual on-aircraft fuselage or wing panel.

Scope and Objective of the Parametric Study

The purpose of this paper is to identify and isolate several key parameters controlling the structural efficiency of skin-stringer compressive panels meeting a given level of damage tolerance. This study uses a compilation of available three-stringer compression-after-impact data, and thus is not a designed experiment to isolate particular variables. Nonetheless, a study of the available data combined with limited numerical verification allows certain conclusions to

be drawn and improvements in methodology to be discussed. A list of parameters and their studied ranges are shown in Table 1. A schematic of a typical I-beam skin-stringer cross-section is shown in Figure 1, and representative tape- and rod-reinforced hat sections shown in Figure 2–4. The following sections of this paper describe the experimental and numerical results, and provide a summary discussion and conclusions.

Experimental Results

This section is separated into discussions of impact survey and compression testing results. The three-stringer panel configurations studied in this paper are described in Table 2. Note that the nomenclature was chosen in order to efficiently capture the state of the parametric variables.

Damage Resistance

Impact surveys were conducted on a variety of three-stringer panels using apparatuses such as that shown in Figure 5. The drop tower drops a 25-lb (11.3 kg) mass that has a 0.5 inch (0.5 mm) spherical radius on the impactor. The panels are clamped to a table using the potted ends for panels to be tested later or wooden end supports for the damage survey panels. Impact surveys described in this paper were conducted at Bell Helicopter (Fort Worth, TX) and in the NASA Langley Research Center (LaRC) Structural Mechanics Laboratory. These tests were performed without dynamic instrumentation. Impact locations in the surveys were made along the lengths of the specimens without regard to rib support location. During these impact surveys, a number of widthwise locations were hit — typically the skin, mid-stringer, flange termination, plank ramp, and/or web–skin intersection. The results of all impact events were then judged visually by engineering and in some cases Government representatives, and a somewhat

subjective determination was made of the threshold of visibility. Dent depth was not measured. Future testing would benefit both from instrumentation and careful control of impact location relative to rib spacing, clamping, and stiffness.

Representative examples of survey panels are shown in Figures 6 and 7. Contact pulse-echo C-scans (color maps of ultrasonic attenuation) were performed on each impact site and the perimeter of the maximum delaminated area marked in pen. In some cases, the area and aspect ratio of this marked region was measured using a planimeter. The panel descriptions, compression test results, and areal characterization of the impact damage zones (as measured on the impact survey panels, not on the test specimens themselves) are given in Table 3. As a general observation from the survey panels, it is apparent that material system and geometric configuration had the largest influence on damage resistance. The combination of geometric configuration and end support essentially defined the boundary conditions for the impact event.

Finally, for the numerical modeling effort reported later in this paper, additional ultrasonic work was done: time-of-flight (TOF) measurements. These measurements were performed only on the damage sites chosen for analysis in order to discriminate between the individual delaminations. Further discussion of these data is reserved for the subsequent numerical results section.

Compressive Strength-After-Impact

A typical three-stringer compression test specimen is shown in Figure 8. Carbon/epoxy doublers 4 inches (102 mm) long were bonded to the stringer caps and skin outer mold line (OML) opposite the plank regions, and on the inside of the caps/flanges of the stringers. The ends were potted in RP1220 potting compound, 1 inch (25 mm) thick, by the Bell Helicopter Methods and Materials Lab. The potting was restrained in an aluminum frame made of 1 × 1

inch (25 × 25 mm) bar. The potted ends were then ground flat and parallel to a tolerance of 0.005 inch (0.13 mm). Various configurations of strain gage, transverse LVDT, and Moiré interferometry instrumentation were used. The specimens were tested either in the Bell Helicopter Mechanical Test Lab or the NASA Langley Research Center Structural Test Lab. A typical test configuration is shown in Figure 9.

Compression test results for each specimen are summarized in Table 3. Comparing results for the I-stiffened panels IT1A and IT1B made from Hexcel 3501-6 resin system indicates that interleaving adhesive layers between the local 0-deg plies added to the panels at the stiffeners (see Figure 1) and the continuous ±45-deg layers in the plank region of the skin increased the failure strain by over 1200 $\mu\varepsilon$. However, a change in plank and stringer configuration (IT1B to IT2B) decreases the failure strain by 1100 $\mu\varepsilon$. Changing from the untoughened 3501-6 resin system to the first-generation toughened 8552 resin (but without adhesive interlayers) resulted in a much higher BVID threshold (500 in·lb (56 J) for IT1B versus 1000 in·lb (113 J) for IT1C), but also a larger damage area (noted by engineers but not quantified in the IT1B data in Table 3). Thus the failure strain for the IT1C panels was 1600 $\mu\varepsilon$ lower than IT1B and also somewhat lower (337 $\mu\varepsilon$) than IT1A. Changing to the E7T1-2 toughened resin system in the panels with an I-stiffener configuration (IT1D versus IT1C) yields somewhat better results (perhaps 620 $\mu\varepsilon$) relative to 8552, but still with a much higher BVID threshold. Note that while higher BVID thresholds are desirable from an operational and supportability standpoint, the toughened resins are penalized due to the visual-inspection-based BVID qualification criterion.

Changing the reinforcement type in the soft skin/plank/hat-section configuration from tape to carbon rod reinforcement (HT to HR) yields mixed results. A detailed examination of the

rod-reinforced hat-section panels indicated that the rods in the first layer of the subcomponents made from 8552 resin system (HR1C) were fractured by the 550 in·lb (62 J) and 1200 in·lb (136 J) impact events. When impacted with 250 in·lb (28 J) of energy to obtain BVID, the rod-reinforced hat-section panel made from E7T1-2 resin system and with a (0/12/0) skin layup (HR3D) did not have fractured layers under the impact site. However, when the (1/16/2) skin layup was used (H*1*), both 8552 and E7T1-2 panels generally showed high failure strains when the plank region was not severely impacted, and low strains to failure when it was. Similarly, in the plankless hard-skin/hat configurations (HT4* and HT5*), the harder the skins, the lower the failure strains. Finally, it is noted that the tougher 3900-2 and 5276-1 resins outperformed the less tough 8552 resin system in the hard skin configurations; and the plankless designs, overall, did better than the discretely stiffened soft-skin/plank configurations (i.e., internal ply dropoffs in planks caused pseudo-free-edge/Poisson effects that were detrimental to skin compressive stability.

Typical strain results for the I- and hat-stiffened panels are shown in Figure 10a through Figure 10f. Strain gage results for Specimen IT1D0, an undamaged I-stiffened panel, are shown in Figure 10a for the centerline cross-section and Figure 10b for a cross-section at the quarter point. Figure 10a indicates a small amount of bending in the center and one side stiffener and no bending in the skin. The results shown in Figure 10b for a cross-section located at the quarter point indicate bending in the skin and no bending in stiffeners. Strain gage results for Specimen IT1D2, a panel that has been impacted with a 1000 in·lb (113 J) of energy near the skin and ramp intersection, are shown in Figures 10b and 10c. Results shown in Figure 10c, for a cross-section located at the center of the specimen, indicate bending in the skin and stiffener adjacent to the impact site. Results shown in Figure 10d for a cross-section located at the quarter point indicate

some bending in the skin and stiffener in the bay adjacent to the impact site. Strain gage results for a hat-stiffened panel, Specimen HT1D1, are shown in Figures 10e and 10f. This panel was impacted with 400 in·lb (45 J) of energy on the ramp between the hat flange and the skin to give a BVID on skin side. Strain gage results shown in Figure 10e indicate bending in the skin on the impact side and also in the center stiffener. The results at the quarter point cross-section, shown in Figure 10f, indicate bending in the center stiffener and a smaller amount of bending in the outside stiffener. The local Moiré fringer pattern at the impact site of specimen IT1D2 at a load of 328 klbf (1.46 MN), with the delamination perimeter superimposed over it, is shown in Figure 11. Note the high local gradients in out-of-plane displacement due to both fiber damage from the indenter and delaminated sublaminate buckling.

Typical failures for the I- and hat-stiffened panels are shown in Figure 12a through Figure 12h. The failure of undamaged Specimen IT1D0 is shown in Figures 12a and 12b. Figure 12a shows the failure on the skin side of the test specimen, while the opposite side is shown in Figure 12b. The I-stiffeners have failed as shown in Figure 12b. The failure of Specimen IT1D2 is shown in Figures 12c and 12d. The failure of the skin side shown in Figure 12c has the same pattern as the undamaged specimen shown in Figure 12a of two failure bands or branches merging into a single branch and then extending through the impact site. The failure on the stringer side is shown in Figure 12d. Two stringers have failed at one location while the third stringer failed at two locations and all of the stringers have delaminated from the skin for the full length of the test area. The failure of Specimen IT1D1 is shown in Figures 12e and 12f. This specimen was impact damaged with 1000 in·lb (113 J) of energy at two locations as shown in Figure 12e. The impact sites were on the ramp of the center stiffener at a quarter of the length and on the centerline of the skin, located at the quarter point from the opposite end. The panel

failed through the damage on the ramp of the center stiffener. Each stringer failed at one location as shown in Figure 12f. The failure of the damaged hat-stiffener specimen is shown in Figures 12g and 12h. Although the skin has many branches to the failure, none of the branches intersect the impact damage. All of the stiffeners failed as shown in Figure 12h and also delaminated at various places between the stiffener flange, the plank runout, and the skin.

Numerical Results

Global finite-element models were built at NASA in order to correlate the observed geometrically nonlinear test results with numerical models that are suitably accurate yet yield efficient elastic response (i.e., strain and displacement) prediction. Global, local, and/or substructured (i.e., fine-grid) models were built at Bell in order to predict ultimate compression strength after impact. The objectives of the NASA and Bell modeling were different, and the results are discussed separately in the two following subsections.

Global Elastic Response Modeling

The finite-element mesh for an I-stiffened panel (Specimen IT1D0) is shown in Figure 13, and the mesh for the hat-stiffened panel (Specimen HT1D1) is shown in Figure 14. The meshes shown in Figures 13 and 14 reflect the actual panel dimensions. Solutions from NASA were generated using the STAGS (STructural Analysis of General Shells) Version 3.0 finite-element program [11]. MSC/PATRAN™ *was used for pre- and post-processing. The STAGS models used Element 410, a four-node quadrilateral element. The applied boundary conditions for the two global models are shown in Figure 15.

---

* MSC/PATRAN™ is a trademark of MSC Software Corporation, Los Angeles, CA.

Comparisons of measured response and STAGS predicted displacements and axial

strains, for selected locations, are shown in Figures 16a through 16d for Specimens IT1D0 and

IT1D2 and Figure 17 for Specimen HT1D1. The end shortening of specimens IT1D0 and IT1D2

as a function of applied load are shown in Figure 16a. The predicted end shortening is also

shown in Figure 16a. The impact damage does not affect the axial stiffness of specimen IT1D2.

Disregarding the offset shown in the experimental results, there is a good comparison between

the predicted and experimental results. The out-of-plane displacement at the center of the

specimens, on the top of the stiffener, is shown in Figure 16b for Specimens IT1D0 and IT1D2.

The predicted displacement at the panel center is also shown in Figure 16b. The out-of-plane

displacement (filled squares) for the damaged panel (IT1D2) exceeds the displacement for the

undamaged, which would be expected since the impact damage is adjacent to the center stiffener.

The out-of-plane displacement for the undamaged panel is less than predicted, as shown in

Figure 16b. The predicted and experimental strain on the center stiffener and skin at the quarter

point in length is shown in Figure 16c. The experimental strain exceeds the predicted strain at

failure by approximately 1000 $\mu\varepsilon$. Very little bending is indicated, at this point in the panel, in

either the predicted or the experimental strains. The predicted and experimental strain in the

center of the skin at the quarter point in the length is shown in Figure 16d. The test results

indicate some bending in the skin at the noted point. The average experimental strain exceeds

the predicted strain by approximately 2000 $\mu\varepsilon$. The predicted end shortening for a hat-stiffened

panel identical to Specimen IH1D1 is shown in Figure 17. The experimental results for

specimen HT1D1 are also shown in Figure 17. The test panel appears to have a lower stiffness

than the panel in the analysis, since the predicted values for strain and deflection are less than the

test values.

The predicted initial buckling load for an I-stiffened panel, Specimen IT1D0, and a hat-stiffened panel identical to Specimen HT1D1 was 693 klbf (3.08 MN) and 669 klbf (2.98 MN), respectively. Since the predicted buckling load is more than 150% of the failure loads, failure by global buckling was not considered further.

Fine-Grid Strength-After-Impact Modeling

The objective of the fine-grid strength-after-impact modeling was to predict the maximum load carried by the three-stringer panels. The following three subsections will (a) overview the general numerical method, (b) describe the typically observed behavior for these three-stringer panels, and (c) present the numerical results.

General Numerical Method. Finite-element analysis performed at Bell used MSC/NASTRAN™ [*]Version 70.5 solution 106 [12]. MSC/PATRAN™ was used for pre- and post-processing. The NASTRAN™ CQUAD4, RBE2 and CGAP elements were the primary elements used. Microsoft® Excel[†] Version 7.0 spreadsheets—developed under a Rotorcraft Industry Technology Association project [13]—were used to automate the most labor-intensive aspects of the local modeling and/or substructuring effort. For this CAI study, six different three-stringer panel configurations were modeled. The Excel spreadsheets, collectively referred to as the Structural Laminate Impact Computations (SLIC), automatically build MSC NASTRAN™ geometric nonlinear finite-element models that capture the impact damage state

---

[*] MSC/NASTRAN™ is a trademark of MSC Software Corporation, Los Angeles, CA.

[†] Microsoft® Excel is a registered trademark of Microsoft Corp., Redmond, WA.

with multiple layered plates tied together with either rigid body or compression-only gap contact elements. This approach makes several assumptions:

1. No delamination growth occurs prior to failure.

2. For damage that occurred directly on plank transition areas such as those shown in Figures 1–3, open-hole compression (OHC) mean failure strain captures the local pseudo-free-edge effects of ply dropoffs.

3. For panels that do not contain internal ply dropoffs, such as the hat-stiffened uniform skin panels as shown in Figure 4, an unnotched laminate compression strain allowable was used to establish the point of failure (for these panels, the hat flange drops off abruptly and this geometry was adequately captured in the finite-element model mesh).

4. The state of damage is repeatable (i.e., identical impact energy and location on an identical panel, produces the same state of damage, and the test panels were assumed to have the same damage state as the damage survey panels even though boundary conditions including the proximity and degree of end support most likely varied).

5. Material response is assumed linear to failure, and geometry is the only contributor to nonlinearity.

The local damage state used in the modeling was determined via contact pulse-echo ultrasonic time of flight (TOF) measurements on the appropriate impact energy and location on the damage survey panels. These scans provide data that shows the extent and depth of each delamination. Typical TOF scan examples are shown in Figures 18 and 19, Figure 18 being a

relatively large delamination in an 8552 I-stiffened panel, and Figure 19 being a much smaller delamination in a tougher 3900-2 resin-system hard-skin/hat configuration. Since the largest delamination is typically on the back side of the panel, one such scan provides all the information required to define the shape, orientation, and depth of all the delaminations. The color scale on the scan is the time required for the ultrasonic wave to bounce off and return from the first interface in the laminate. The scale is proportional to depth or thickness (note that the edges of the dropped 0° plies in Figure 18 show up as a change in depth as the delamination follows the plank contour). The outer surface on the panel must be smooth in order to provide a consistent reference plane for automated TOF scans. Several damage survey panels had a rough outer surface and could only be hand scanned. Sufficient data was gathered, however, with hand scans to proceed with the SLIC analysis.

As shown in Figures 20 and 21, the element density for the global portion of the model was typically about 0.4 inch to 0.75 inch (10 mm to 19 mm) using CQUAD4 elements. The global/substructured model of an I-stiffened three-stinger panel is shown in Figure 20, while Figure 21 shows a hat-stiffened panel. In the proximity of the impact site, the element density is increased to about 0.10 inch (2.5 mm). This fine-meshed region is duplicated into multiple stacks of plates that align with each other through the thickness and encompass the entire damage region and extend out some distance beyond, as shown in Figure 22. Each plate layer represents a sublaminate whose boundaries are defined by the delamination interfaces. The extent of damage at each sublaminate interface can be independently defined as a unique ellipse oriented at an alignment angle. SLIC automatically generates a full or truncated ellipse. Any other shape can be transferred from the scans by manual editing. CGAP gap elements are inserted inside the ellipses and transfer only compression forces that prevent the sublaminates

from passing through one another. RBE2 rigid body elements are then used to connect the sublaminates in the remaining fine meshed area outside the damage zone.

The models can be set up to run two ways. The first is to run a coarse grid global model with local damage element softening only. A moment fringe plot is then set up in PATRAN™ with the fringe bounds set very tightly around zero. A positive moment then plots as one color, while the negative moment region plots as another. The moment inflection lines are then obvious. The local model is then built and run separately using the moment inflection lines as a simplified loading boundary. This method is illustrated in Figure 23. The total number of elements for a global three-stringer panel model using this technique is around 5 000 to 10 000 with around 20 000 to 30 000 degrees of freedom (DOF). The run times are between 30 and 100 central processing unit (CPU) minutes. The local model then contains about 10 000 to 20 000 elements with 20 000 to 80 000 DOF, and the run times go from 100 to 400 CPU minutes. This method requires a careful consideration of local model boundary stiffness, especially for an impact at an edge of a flange or a ramp. It works best for damage isolated in the center of a skin panel.

The second technique is to run the combined local and global model together, i.e., substructuring. This is the technique used in the models shown in Figures 20 – 22. The substructuring version of SLIC builds one model and includes a mesh transition region or band between the multilayer fine-grid mesh and the surrounding single-layer coarse elements. SLIC generates a PATRAN™ session file that fully generates the combined model in approximately 10 to 20 minutes work time. This technique contains between 50 000 to 100 000 elements with 70 000 to 120 000 DOF and runs in about 500 to 1000 CPU minutes.

In both approaches, the elements at the immediate impact site location are softened to represent local matrix cracking and fiber damage. This local impact damage zone is idealized as a cone that gets progressively larger away from the impact side. The 0.5-inch (13-mm) indenter tip radius and the dent depth, if recorded, determine the impact diameter of the cone. The cone angle is then assumed to be 45-deg. The model now contains two major zones where strain or stress concentrations can develop. The first is along the outside edges of the delaminations where local bending strains can become high, and the second is at the edge of the local impact site where load wants to locally redistribute around the soft spot.

The geometrically nonlinear NASTRAN™ solution 106 is typically set up to run in 10 load increments to 100% of the expected failure load and then 10 more increments to 150%. The model will usually reach a point where the solution becomes unstable. This point may not be the actual point of final collapse. The next step is to query PATRAN™ for the highest axial strain magnitude (i.e., in the direction of loading). Once the element is identified that has the highest laminate-level axial strain magnitude, the maximum zero degree ply strain is calculated. This strain is then compared to an average room temperature allowable. If this strain is lower than the allowable, the model must be rerun with either finer load increments or a finer mesh in order to get the model to run stable for a higher load. If the model strain is higher than the allowable, the applied load is reduced by the ratio of worst minimum zero ply model strain over the strain allowable.

Typically Observed Behavior. The typically observed failure modes for these three-stringer panels are various types of buckling and load redistributions leading up to a final compressive strength failure. Pure buckling and strength modes were not found in the three-

stringer panels that were evaluated. Three-stringer panels contain multiple load paths. If a web buckles, the stringers can take additional load. If a sublaminate buckles, other parallel sublaminates will also react additional load. As more and more of the redundant load paths become soft from buckling, the remaining strain energy concentrates at an increasing rate into the last stable load paths. Finally, the point of local fiber stability is exceeded and a 0-deg compressive (or "kink-band") failure is initiated. Energy is released by the fiber failure and immediately overloads the adjacent fibers, leading to a sudden collapse. This nonlinear phenomenon is illustrated in Figure 24 (and captured experimentally in the Moiré fringe pattern shown in Figure 11), and the numbered events may also be related to the exploded view of the substructured model in Figure 22. The nonlinear NASTRAN analysis will reproduce the progressive sublaminate buckling phenomenon. Numerical instabilities resulting in nonconvergence, and suspicious failure modes (and/or locations) were often encountered, and some judgement was required in recognizing them and correctly adjusting the solution step size in order to overcome them. By checking the post-processed peak axial strains at the end of a solution, the load and location at which the final kink-band failure occurs may be estimated. The locations of these peak strains, within the unbuckled sublaminate were observed to vary from one configuration to another, but were found either at the center of the impact site or near the edge of a delamination in a successfully converged run.

Detailed Parametric Model Results. Table 4 compares the experimental results to the predicted failure load based on comparing peak local/substructured model axial strains with the noted open hole compression (OHC) or no hole compression (NHC) mean room temperature ambient (RTA) strain allowable. In general, the numerical agreement, within 20% in five of six cases, is considered very good. While *a priori* knowledge of the experimental results was

available for this modeling exercise, it only influenced the overall direction of the model-building in the HT1D case, and blind comparisons with test data will be performed in the near future. The single buckling failure prediction (HT5C) illustrates the caution required in interpreting the nonlinear model results. As mentioned previously, a pure buckling failure is indicative of a poorly converged or too coarsely meshed solution, and thus the tabulated result for case HT5C should actually be discarded (it is only included to illustrate this point) and the model re-run. Note also that the HT5C solution is the only unconservative numerical result.

There are several possible ways to improve the accuracy and reliability of this numerical strength prediction method. Certainly characterizing with TOF measurements the delamination actually present in the test panel would be an obvious improvement over the use of survey panel impact sites and the assumption that the test panel damage was identical. A statistically significant study of impact damage variability would also be useful. In addition, a pure compression strain allowable was used in this study with a simple maximum strain failure criterion. This was done in spite of the fact that the critical sublaminate often exhibited large bending strains (and thus interlaminar shear stresses) and in-plane shear stresses as well, depending on local geometric details. Thus, another obvious improvement would be to use a failure criterion with compression-shear interaction.

Summary

This summary is separated into subsections: (a) discussing the merits and limitations of the observed results, and (b) listing the conclusions.

Discussion

A compilation of existing experimental three-stringer impact resistance and compression after impact strength results allows several key design parameters to be evaluated. Since this study was not a designed experiment, statistically rigorous conclusions were not necessarily possible. Nonetheless, certain useful engineering assessments were able to be made. Most of these conclusions merely confirmed common existing assumptions, such as the facts that tougher resins yield smaller damage zones and higher detection thresholds, hard laminates have more severe stress concentrations/strength knockdowns, and hat sections are more stable/efficient that I-stiffeners. Since the local details of the damage zone strongly influence strength, careful attention (perhaps in the form of dynamic instrumentation and thorough control of clamping and impact location relative to panel edges) must be paid to boundary conditions for the impact event. Finally, simply compiling and publishing this relatively large experimental data base (39 test panels) for future reference is useful to some extent.

A practical global-local modeling technique was utilized in order to capture observed experimental elastic response and predict structural failure. An obvious improvement to this technique would be a failure criterion with compression-shear interaction. In the future, this numerical technique will allow the user to identify critical damage sites and estimate strength with damage prior to testing.

Finally, a statistically significant study of impact damage variability would be useful from both a certification/qualification support basis, and a confidence-in-modeling standpoint. Another certification/qualification issue highlighted by this study is the strong sensitivity of strength to damage zone size and, thus, to the definition of BVID. Hence, there seems to be merit in considering damage resistance criteria alternatives to BVID.

Conclusions

1. Material system and geometric configuration (i.e., the boundary conditions for the impact event) had the largest influence on damage resistance.

2. Location and extent (relative to critical geometric details such as ply edges) of the damage zone influenced the sublaminate buckling behavior, failure initiation site, and compressive ultimate strength.

3. Skin sublaminate stability and compression strength control structural failure.

4. Planks exhibited detrimental pseudo-free-edge/Poisson effects on strength.

5. Tougher resin systems had to be hit harder to reach their BVID threshold.

6. Since the tougher resin systems were hit harder, their CAI strength was similar to the more brittle systems.

7. Rodpacks only improve structural efficiency in concert with (0/12/0) skins and webs.

8. Hat stiffeners are more stable than I-stiffeners.

9. The nonlinear global-local finite-element-based strength predictions match the test data fairly well (i.e., within 20%).

Acknowledgements

References

[1]   USAF Guide Specification for Aircraft Structures, AFGS-87221A (June, 1990).

[2]   FAA Advisory Circular No. 20-107A, Composite Aircraft Structure (April 1984).

[3]   Jaeb, J. R., "Standardization of Composite Damage Criteria for Military Rotary and Fixed Wing Aircraft," Aerospace Industries Association Material and Structures Committee, Washington, D.C. (Dec 1994).

[4]   Williams, J. G., Anderson, M. S., Rhodes, M. D., Starnes, J. H. Jr., and Stroud, W. J., "Recent Developments in the Design, Testing, and Impact-Damage Tolerance of Stiffened Composite Panels," *Fibrous Composites in Structural Design*, E. M. Lenoe, et al., eds., (Conf. Proc., San Diego, CA, 14–17 November 1978), Plenum Press (1980), pp. 259–291.

[5]   Walker, T. H., Minguet, P. J., Flynn, B. W., Carbery, D. J., Swanson, G. D., and Ilcewicz, L. B., "Advanced Technology Composite Fuselage – Structural Performance," NASA CR 4732 (April, 1997).

[6]   Shyprykevich, P., "Damage Tolerance of Composite Aircraft Structures: Analysis and Certification," Proc., ICCM XI, Sydney, Australia (1997).

[7]   Wiggenraad, J. F. M., Aoki, R., Gadke, M., Greenhalgh, E., Hachenberg, D., Wolf, K., and Bubl, R., "Damage Propagation in Composite Structural Elements - Analysis and Experiments on Structures," *Composite Structures*, 36 (1996), pp. 173–187.

[8]   Gadke, M., Geier, B., Goetting, H., Klien, H., Rowher, K., and Zimmermann, R., "Damage Influence on the Buckling Load of CFRP Stringer-Stiffened Panels," *Composite Structures*, 36 (1996), pp. 249–275.

[9]   Greenhalgh, E., Bishop, S., Bray, D., Hughes, D., Lahiff, S., and Millson, B., "Characterisation of Impact Damage in Skin-Stringer Composite Structures," *Composite Structures*, 37 (1997), pp. 187–207.

[10] Falzon, B., and Steven, G., "Buckling Mode transition in Hat-Stiffened Composite Panels Loaded in Uniaxial Compression," *Composite Structures*, 37 (1997), pp. 253–267.

[11] Brogan, F. A., Rankin, C. C., and Cabiness, H. D., *STAGS Users Manual*, Lockheed Palo Alto Research Laboratory, Report LMSC P032594, 1994.

[12] *MSC/NASTRAN Quick Reference Guide, Version 70*, MSC Software Corp., Los Angeles, CA (1998).

[13] Hethcock, J. D., "Strength Determination of Damaged Laminates Using Commercial Finite-Element Model Codes," American Helicopter Society, Stratford, CT (7–8 October 1998).

<div align="center">TABLE 1 – Parametric variables</div>

Parameter	Initial	Intermediate	Intermediate	Intermediate	Final
Stiffener section	I	...	...	...	Hat
Skin layup	$(0/12/0)^a$	$(1/16/2)$	...	$(3/10/2)$	$(10/10/2)$
Plank layup	none	$(4_{RP}/26/4)^b$	$(21/16/2)^c$	$(21/16/2)$	$(35/32/2)$
Resin	3501-6	8552	E7T1-2	3900-2	5276-1
Axial reinforcement	Tape	...	...	...	Rodpack

[a] Number of $(0/\pm45/90)$ plies.

[b] Subscript "RP" denotes rodpack (pultruded carbon rods encapsulated in syntactic adhesive rather than unidirectional tape layers).

[c] Grade 05 FM300 adhesive layers above and below each 0-deg ply pack in plank.

<div align="center">TABLE 2 – Panel configurations</div>

Nomen.	Stiffener	Skin[a,b]	Web[a]	Flange[a]	Plank[a]	Cap[a]	Resin	Tested
IT1A	I, tape	$(1/16/2)$	$(30/10/4)$	$(15/5/2)$	$(21/16/2)$	$(30/10/4)$	3501-6	2
IT1B	I, tape	$(1/16/2)$	$(30/10/4)$	$(15/5/2)$	$(21/16/2)^c$	$(30/10/4)$	3501-6	2
IT2B	I, tape	$(1/16/2)$	$(28/10/4)$	$(14/5/2)$	$(28/16/2)^c$	$(30/10/3)$	3501-6	2
IT1C	I, tape	$(1/16/2)$	$(30/10/4)$	$(15/5/2)$	$(21/16/2)$	$(30/10/4)$	8552	3
IT1D	I, tape	$(1/16/2)$	$(30/10/4)$	$(15/5/2)$	$(21/16/2)$	$(30/10/4)$	E7T1-2	3
HT1C	Hat, tape	$(1/16/2)$	$(0/10/0)$	$(0/10/0)$	$(35/32/2)$	$(36/30/0)$	8552	3
HT1D	Hat, tape	$(1/16/2)$	$(0/10/0)$	$(0/10/0)$	$(35/32/2)$	$(36/30/0)$	E7T1-2	1
HR1C	Hat, rod	$(1/16/2)$	$(0/9/1)$	$(0/9/1)$	$(4_{RP}/26/4)$	$(4_{RP}/9/1)$	8552	2
HR3D	Hat, rod	$(0/12/0)$	$(0/10/0)$	$(0/10/0)$	$(4_{RP}/26/4)$	$(4_{RP}/10/0)$	E7T1-2	4
HT4C	Hat, tape	$(3/10/2)$	$(2_F/8_F/0)$	$(2_F/8_F/0)$	...	$(20_T,2_F/8_F/0)$	8552	3
HT4E	Hat, tape	$(3/10/2)$	$(2_F/8_F/0)$	$(2_F/8_F/0)$	...	$(20_T,2_F/8_F/0)$	3900-2	3
HT5C	Hat, tape	$(10/10/2)$	$(2_F/8_F/0)$	$(2_F/8_F/0)$	...	$(20_T,2_F/8_F/0)$	8552	3
HT5E	Hat, tape	$(10/10/2)$	$(2_F/8_F/0)$	$(2_F/8_F/0)$	...	$(20_T,2_F/8_F/0)$	3900-2	3
HT5F	Hat, tape	$(10/10/2)$	$(2_F/8_F/0)$	$(2_F/8_F/0)$	...	$(20_T,2_F/8_F/0)$	5276-1	5

[a] Number of $(0/\pm45/90)$ plies; tape unless otherwise indicated (RP = rodpack or F = fabric).

[b] One ply of 45-deg fine-grade carbon fabric on IML, and one on OML not shown in layups.

[c] Grade 05 FM300 adhesive layers above and below each 0-deg ply pack in plank.

TABLE 3 – Compression test results

Spec ID	Skin (Msi·in²)	Skin (MPa·m²)	Plank[a] (Msi·in²)	Plank[a] (MPa·m²)	Stringer[a] (Msi·in²)	Stringer[a] (MPa·m²)	Total (Msi·in²)	Total (MPa·m²)	Critical location	Energy (in·lb)	Energy (J)	Damage Area (in²)	Damage Area (mm²)	AR[b]	Orien[b] (deg)	P_{max}[c] (klbf)	P_{max}[c] (MN)	P/EA (µε)
IT1A1	…	…	…	…	…	…	76.03	338	Ramp	550	62.1	…	…	…	…	…	…	3821
IT1A2	…	…	…	…	…	…	76.03	338	Ramp	550	62.1	…	…	…	…	…	…	3538
IT1B1	5.34	23.8	28.83	128	41.86	186	76.03	338	Ramp	500	56.5	…	…	…	…	374.5	1.67	4926
IT1B2	5.34	23.8	28.83	128	41.86	186	76.03	338	Ramp	500	56.5	…	…	…	…	377.4	1.68	4964
IT2B1	4.47	19.9	50.79	226	32.52	145	87.78	390	Ramp	500	56.5	…	…	…	…	348.8	1.55	3974
IT2B2	4.47	19.9	50.79	226	32.52	145	87.78	390	Ramp	500	56.5	…	…	…	…	325.3	1.45	3706
IT1C1	3.65	16.2	44.20	197	35.55	158	83.40	371	Ramp	1000	113	10.62	6852	0.57	0	272.4	1.21	3266
IT1C2	3.65	16.2	44.20	197	35.55	158	83.40	371	Ramp	1000	113	10.62	6852	0.57	0	276.7	1.23	3318
IT1C3	3.65	16.2	44.20	197	35.55	158	83.40	371	Ramp	1000	113	10.62	6852	0.57	0	287.4	1.28	3446
IT1D0	4.68	20.8	15.78	70.2	13.24	58.9	91.75	408	NA	0	0	0	0	NA	NA	431.3	1.92	4700
IT1D1	4.68	20.8	15.78	70.2	13.24	58.9	91.75	408	Ramp	1000	113	2.34	1510	0.80	0	383.4	1.71	4179
IT1D2	4.68	20.8	15.78	70.2	13.24	58.9	91.75	408	Ramp[d]	1000	113	4.00	2581	0.70	0	343.7	1.53	3746
HT1C1	11.29	50.2	47.13	210	27.78	124	86.20	383	Skin	500	56.5	6.64	4284	0.60	45	452.7	2.01	5525
HT1C2	11.29	50.2	47.13	210	27.78	124	86.20	383	Ramp	1200[e]	136	4.64	2994	1.00	0	425.9	1.89	3489
HT1C3	11.29	50.2	47.13	210	27.78	124	86.20	383	Ramp	1200[e]	136	4.64	2994	1.00	0	401.9	1.79	3051
HT1D1	1.17	5.20	23.34	104	9.01	40.1	98.22	437	Ramp	400	45.2	1.28	826	0.88	0	412.5[f]	1.83	4200
HR1C1	…	…	…	…	…	…	72.10	321	Plank	550[g]	62.1	4.70	3032	0.67	0	285.8	1.27	3964
HR1C2	…	…	…	…	…	…	72.10	321	Plank	1200	136	4.70	3032	0.67	0	287.0	1.28	3981
HR3D0	…	…	…	…	…	…	62.50	278	NA	0	0	0	0	NA	NA	420.1	1.87	6722
HR3D1	…	…	…	…	…	…	62.50	278	Plank	250	28.2	…	…	…	0	364.8	1.62	5867
HR3D2	…	…	…	…	…	…	62.50	278	Plank	250	28.2	…	…	…	0	421.5	1.87	6744
HR3D3	…	…	…	…	…	…	62.50	278	Plank	1200	136	…	…	…	0	279.3	1.24	4469
HT4C0	13.35	59.4	…	…	11.73	52.2	25.08	112	NA	0	0	0	0	NA	NA	127.1	0.57	5068
HT4C1	13.35	59.4	…	…	11.73	52.2	25.08	112	Flange	400	45.2	3.80	2452	0.42	0	105.7	0.47	4215
HT4C2	13.35	59.4	…	…	11.73	52.2	25.08	112	Flange	400	45.2	3.80	2452	0.42	0	113.8	0.51	4537
HT4E0	12.65	56.3	…	…	11.27	50.1	23.92	106	NA	0	0	0	0	NA	NA	143.3	0.64	5991
HT4E1	12.65	56.3	…	…	11.27	50.1	23.92	106	Flange	300	33.9	…	…	…	0	138.2	0.61	5778
HT4E2	12.65	56.3	…	…	11.27	50.1	23.92	106	Flange	400	45.2	…	…	…	0	137.4	0.61	5744
HT5C0	32.02	142	…	…	11.73	52.2	43.75	195	NA	0	0	0	0	NA	NA	198.0	0.88	4526
HT5C1	32.02	142	…	…	11.73	52.2	43.75	195	Flange	600	67.8	5.30	3419	0.36	0	145.9	0.65	3335
HT5C2	32.02	142	…	…	11.73	52.2	43.75	195	Flange	500	56.5	…	…	…	0	160.2	0.71	3662
HT5E1	30.92	138	…	…	11.27	50.1	42.19	188	Flange	475	53.7	1.44		0.43	0	191.5	0.85	4539
HT5E2	30.92	138	…	…	11.27	50.1	42.19	188	Hat	450	50.8	…	…	…	0	196.7	0.87	4662
HT5E3	30.92	138	…	…	11.27	50.1	42.19	188	Web	400	45.2	…	…	…	0	190.2	0.85	4508
HT5F1	30.97	138	…	…	11.74	52.2	42.71	190	Flange	500	56.5	2.88	1858	0.38	0	209.0	0.93	4893
HT5F2	30.97	138	…	…	11.74	52.2	42.71	190	Hat	600	67.8	2.82	1819	1.00	0	185.2	0.82	4336
HT5F3	30.97	138	…	…	11.74	52.2	42.71	190	Web	600	67.8	2.18	1406	0.40	0	196.0	0.87	4589
HT5F4	30.97	138	…	…	11.74	52.2	42.71	190	Web	600	67.8	2.18	1406	0.40	0	211.8	0.94	4959
HT5F5	30.97	138	…	…	11.74	52.2	42.71	190	Web	600	67.8	2.18	1406	0.40	0	203.9	0.91	4774

NOTES:

a Sum of three planks or stringers.

b Aspect ratio (AR) is maximum delamination width/length, with the orientation of the length measurement at an angle denoted "orien" relative to the loading direction.

c All tests conducted at room temperature ambient conditions.

d Damage mislocated 0.1 inch (2.5 mm) to skin side.

e Energy level above BVID using the Air Force 1200 in·lb (136 J) impact energy criterion.

f Did not fail through damage area.

g Energy level below BVID in order approximate a less severe criterion (the delamination sizes were the same for both 550 in·lb [62 J] and 1200 in·lb [136 J] impact energy levels).

TABLE 4 – Comparison of FEM and Experimental Results

Panel ID	No. of data points	Material	Critical damage impact energy (in·lb)	(J)	Critical sublam (/tot)	Critical location	Allow local strain (µε)	Test global P/AE (µε)	Predicted failure (% test)	Failure mode
IT1C	3	IM7/8552	1000	136	4/5	plank ramp	-6022	-3343	118	Strength failure at impact site
HT1D	1	IM7/E7T1	none[a]	none[a]	NA	plank	-5794	-4785	109	Strength failure of plank
HT4C	2	IM7/8552	400	45	4/4	skin[b]	-9436	-4376	123	Strength failure at edge of delam
HT5C	1	IM7/8552	600	68	3/4	skin[b]	-9302	-3335	86	Buckling
HT5F.1	1	G40/5276	500	56	3/4	skin[b]	-9061	-4893	114	Strength failure at impact site
HT5F.2	3	G40/5276	600	68	2/4	skin[c]	-8998	-4774	103	Strength failure at edge of delam

NOTES:

[a] Specimen did not fail through impact site; thus, impact damage was not modeled.

[b] Under flange-end

[c] Under web-skin intersection
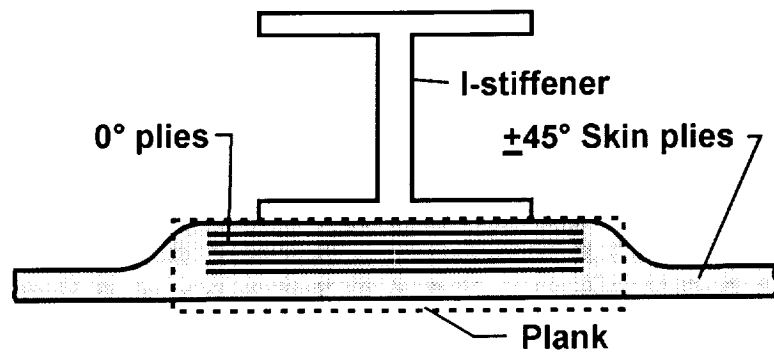
Figure 1. - Schematic of a typical I-beam/plank/skin configuration
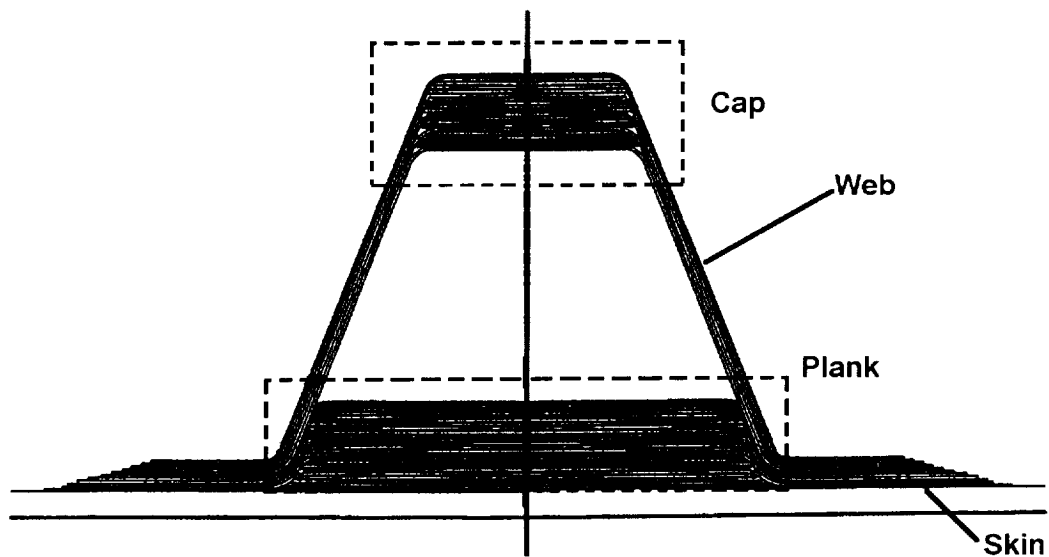
Figure 2. - Schematic of a typical tape hat/plank/skin configuration
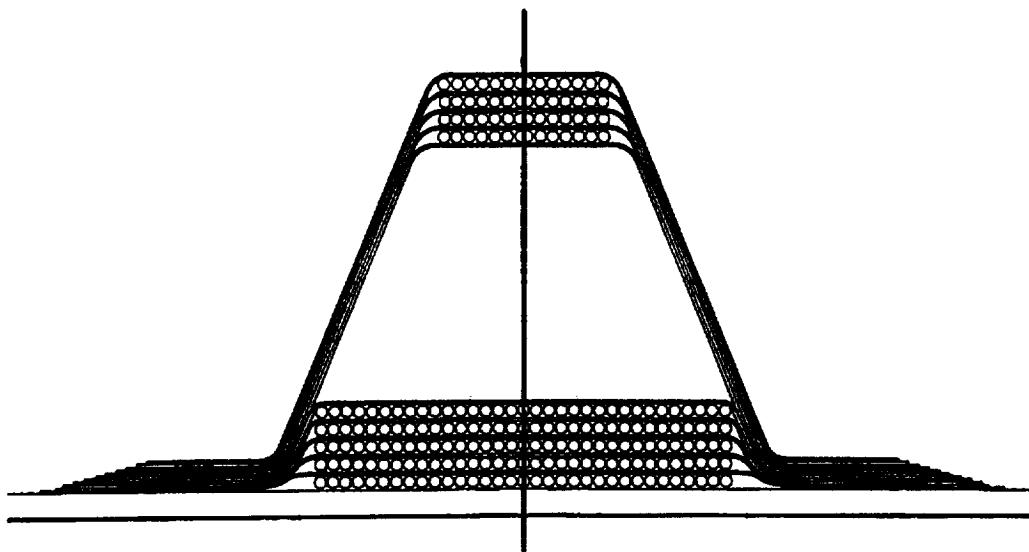
Figure 3. - Schematic of a typical rod-reinforced hat/plank/skin configuration
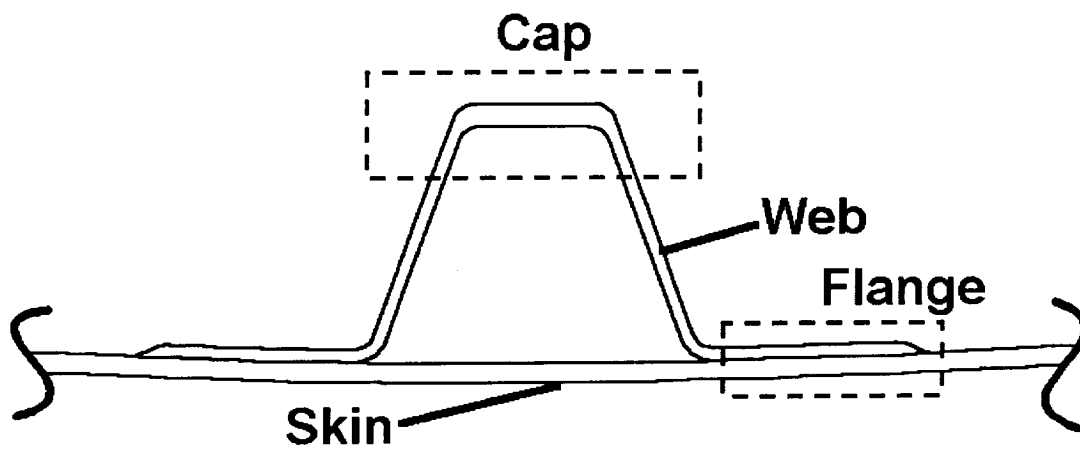
Figure 4. - Schematic of a typical tape hat/skin configuration
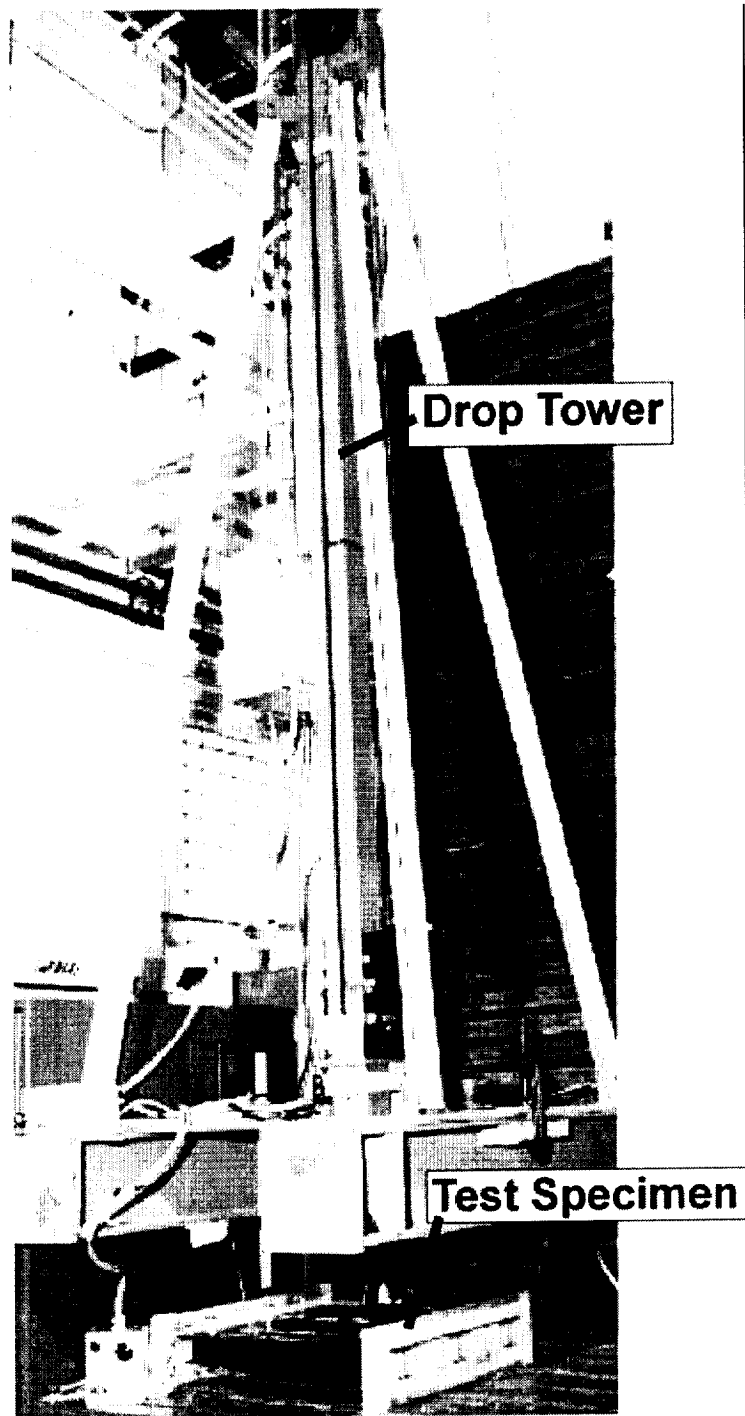
Figure 5. - NASA Langley low-velocity drop tower

I-stiffened panel

Cut on these lines (9 places)
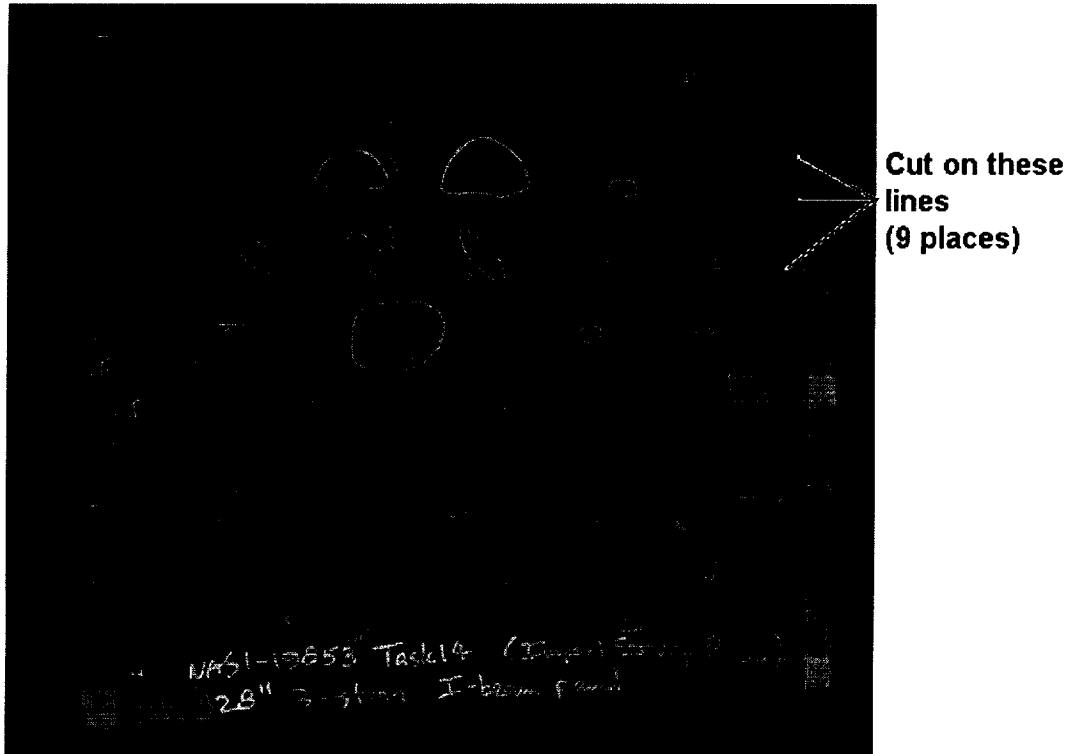
Figure 6. - Three stringer IM7/E7T1-2 I-beam impact survey panel

Hat-stiffened panel

**Cut on lines
(9 places)**
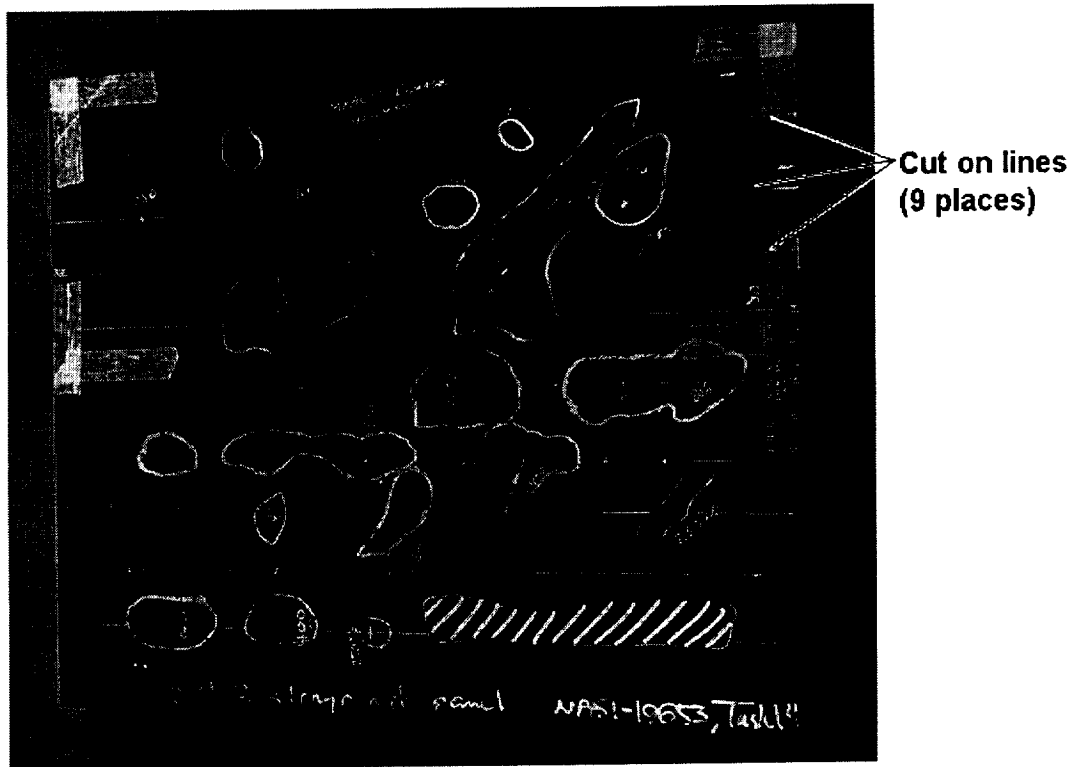
Figure 7. - Three stringer IM7/E7T1-2 tape hat impact survey panel
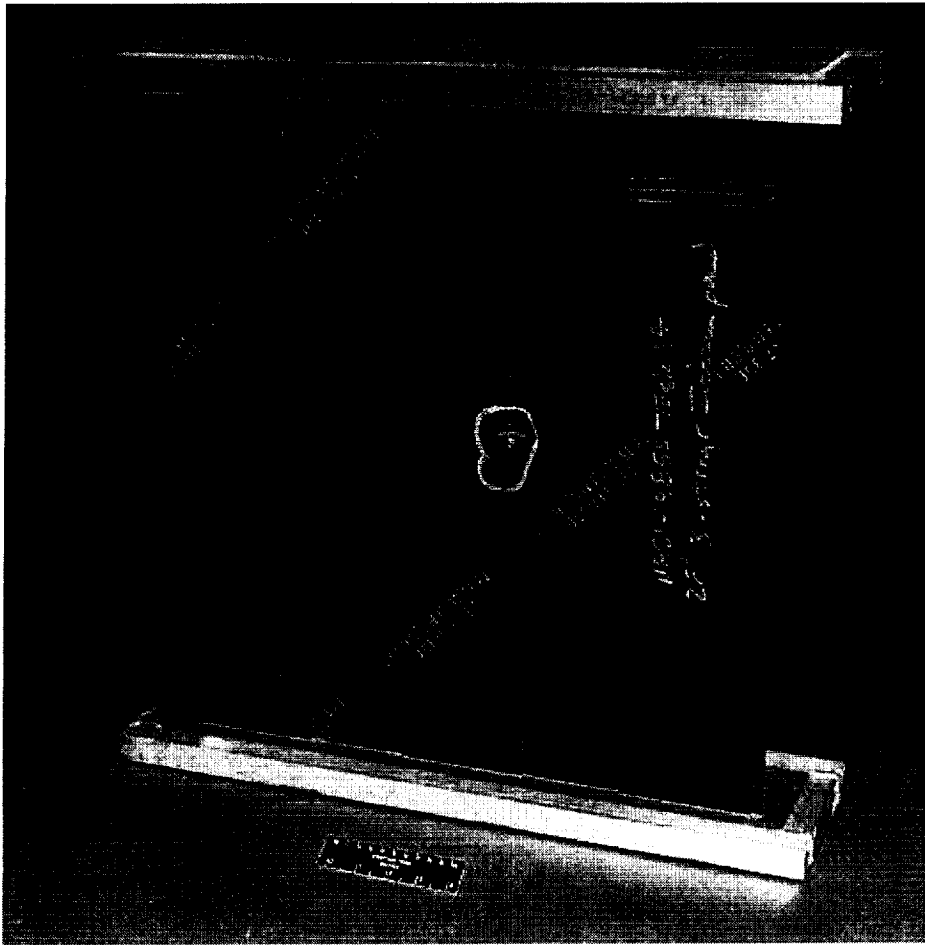
Figure 8. - Typical three stringer compression test specimen
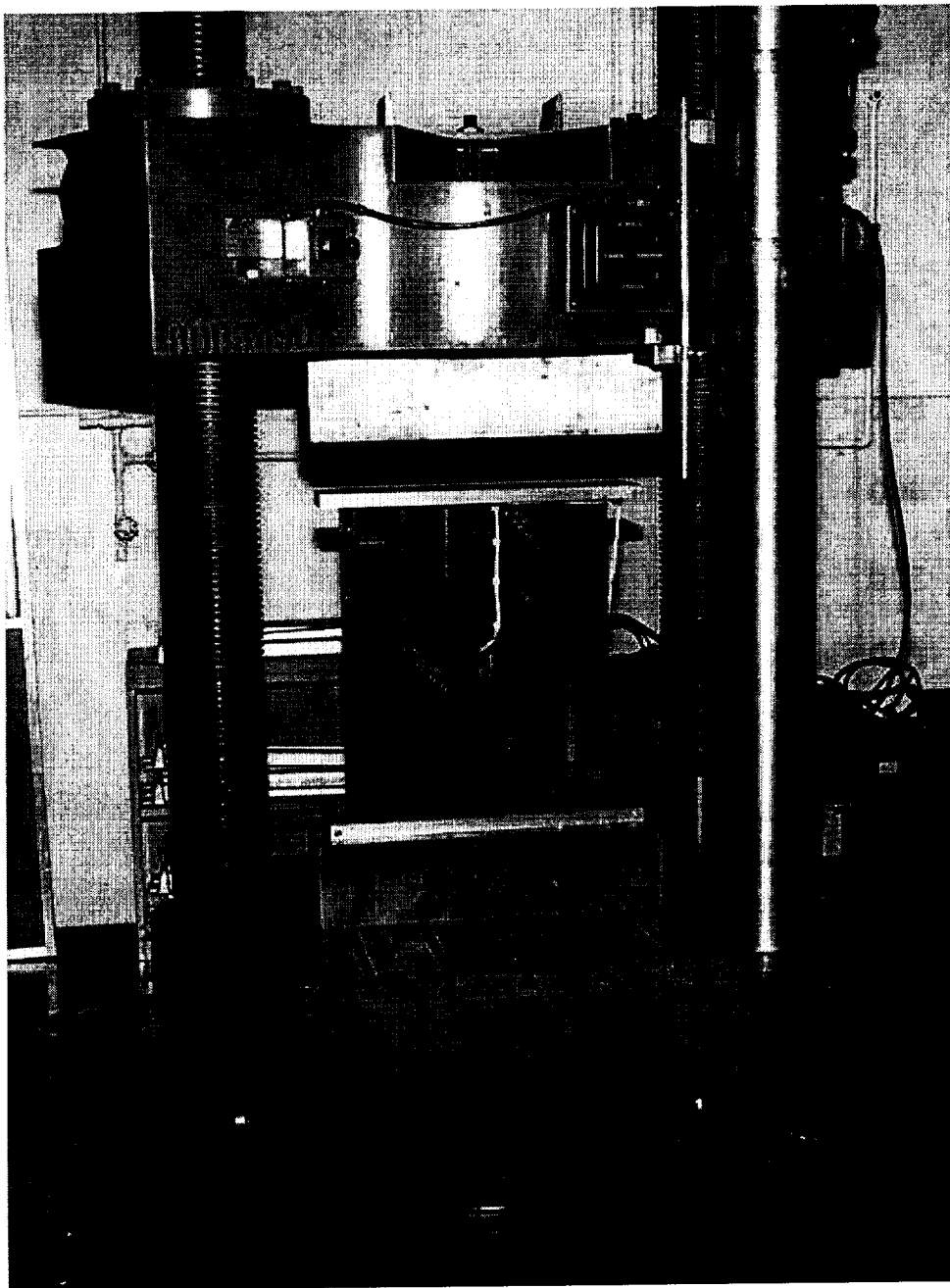
Figure 9. - Typical three stringer compression test set-up
(Bell Helicopter Mechanical Test Lab)
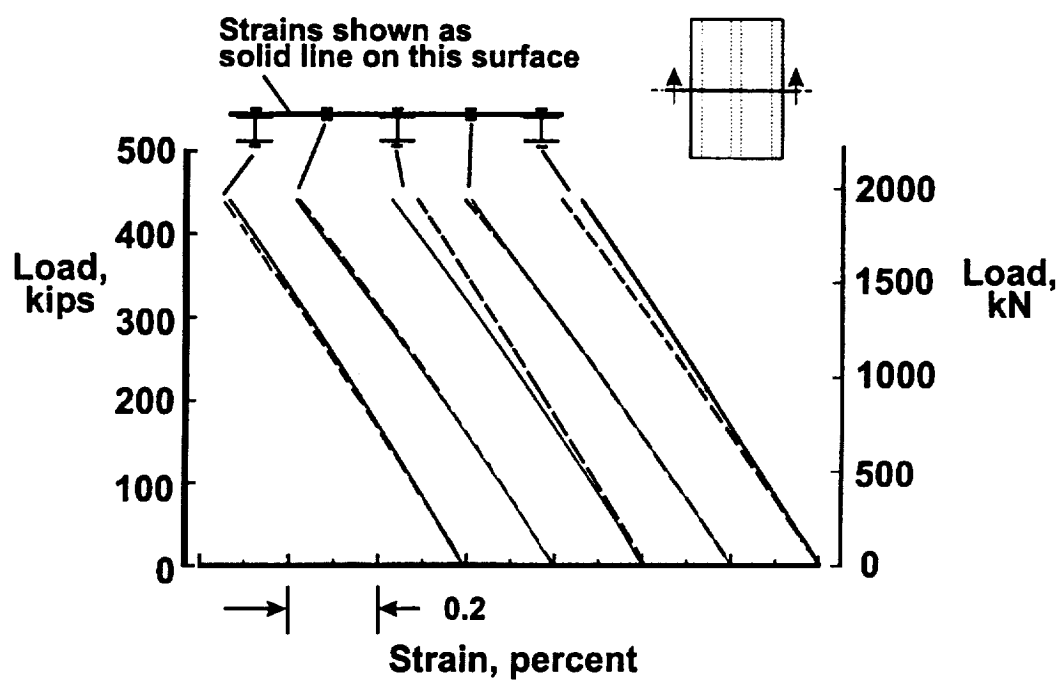
Figure 10a. – Load-strain response at center cross-section of (undamaged) Specimen IT1D0
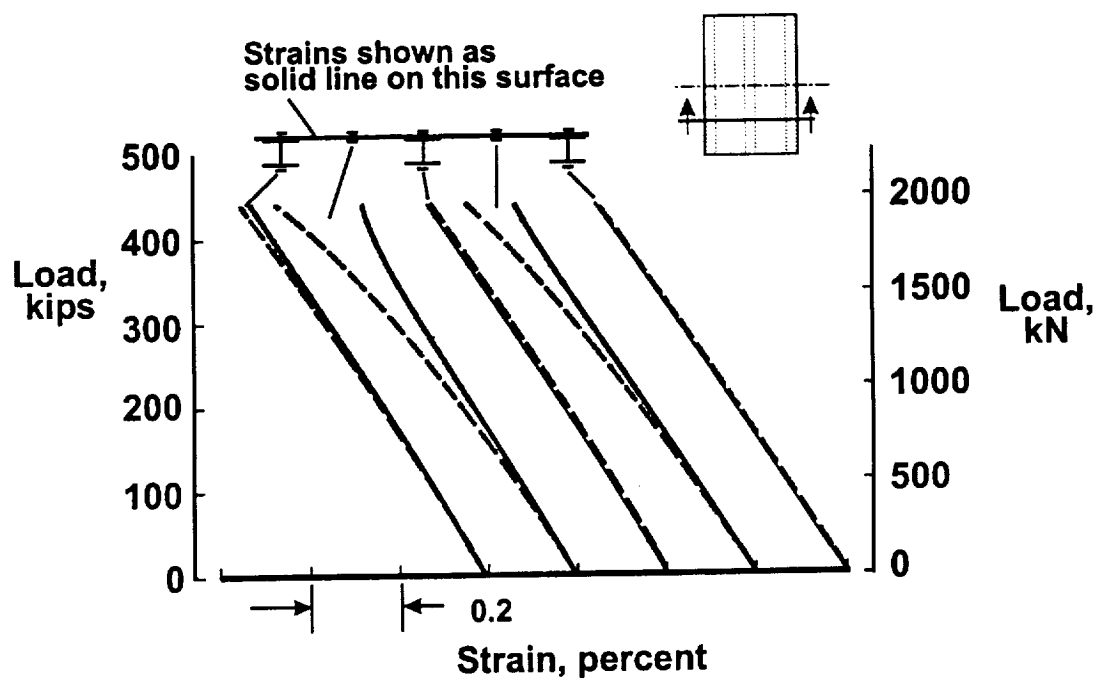
Figure 10b. – Load-strain response at cross-section located at quarter point of Specimen IT1D0
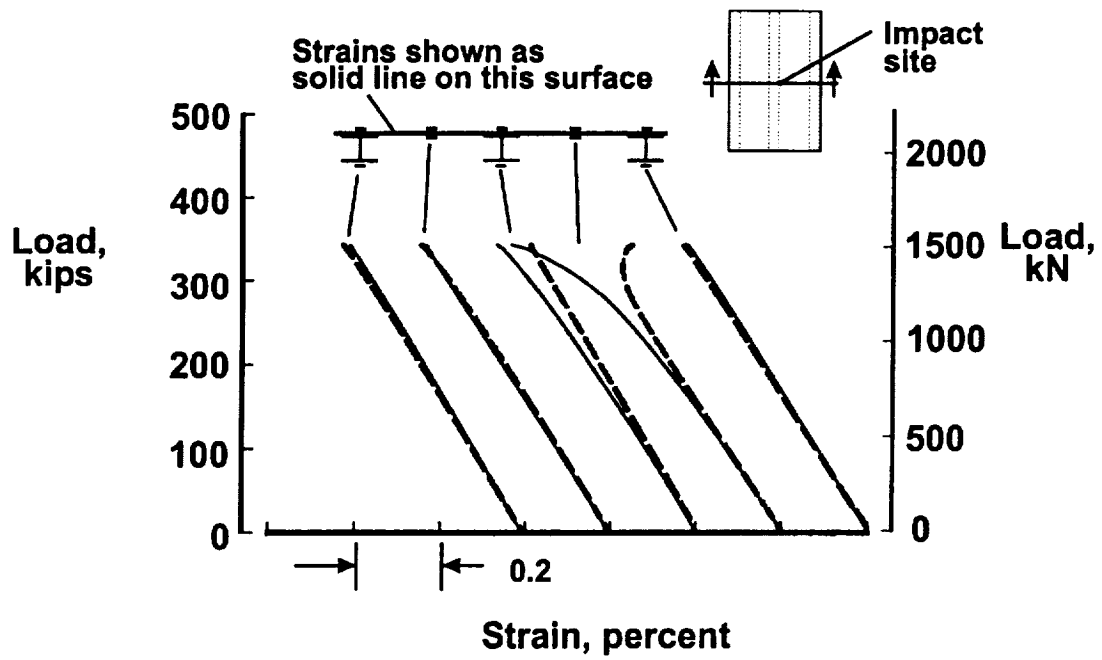
Figure 10c. – Load-strain response at center cross-section of Specimen IT1D2
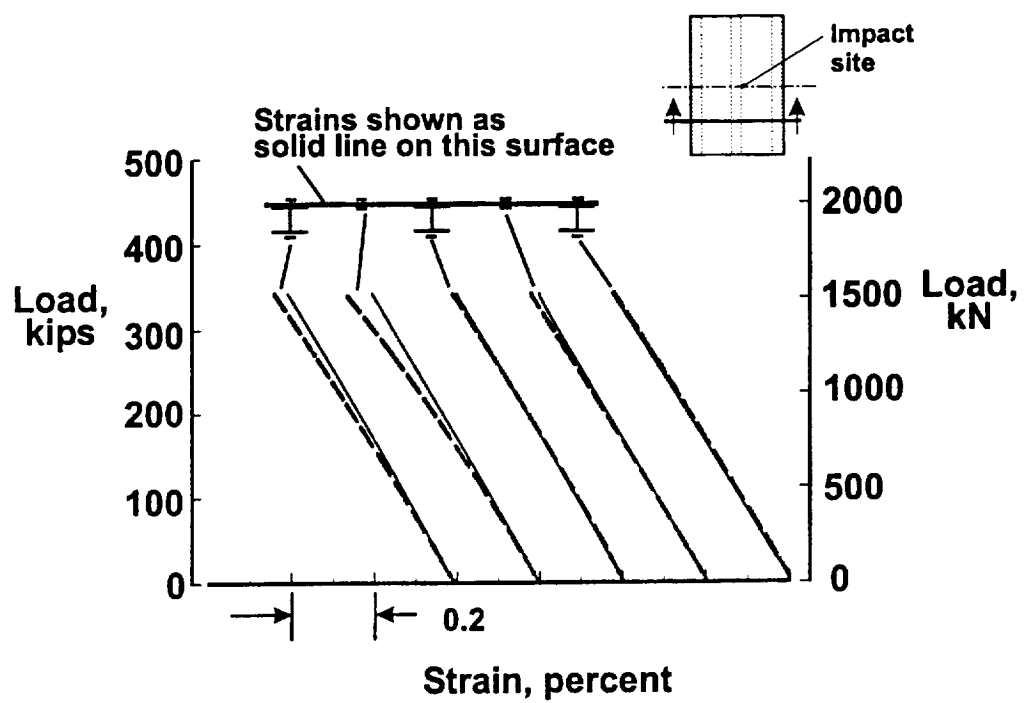
Figure 10d. – Load-strain response at cross-section located at quarter point of specimen IT1D2
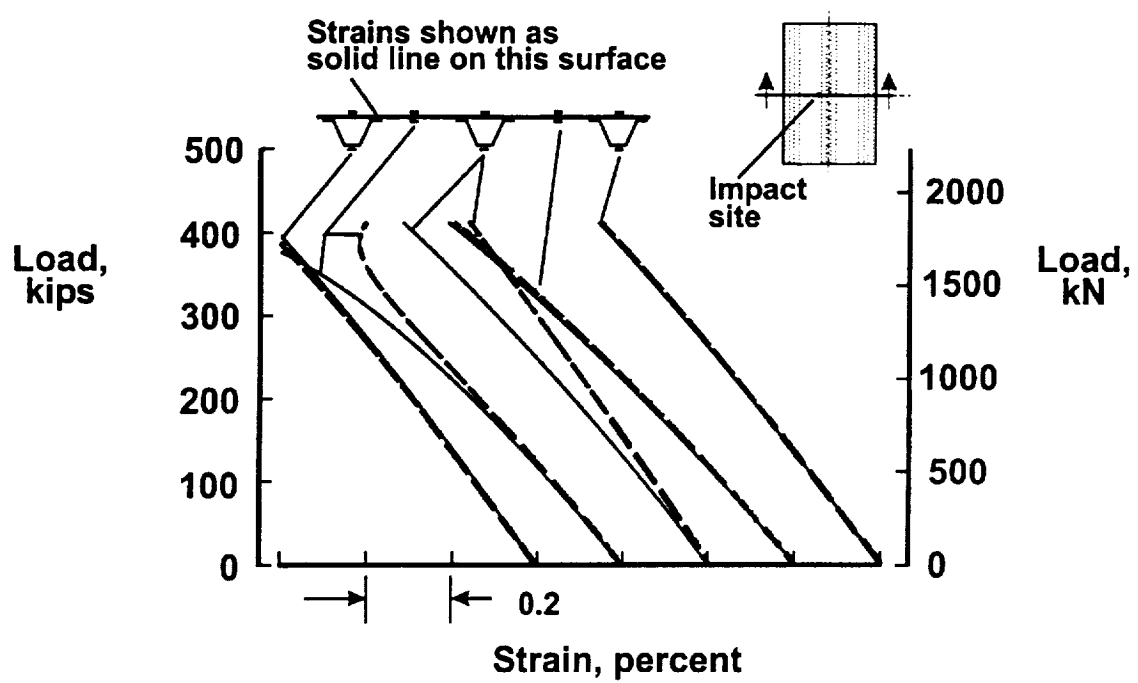
Figure 10e. – Load-strain response at center cross-section of Specimen HT1D1
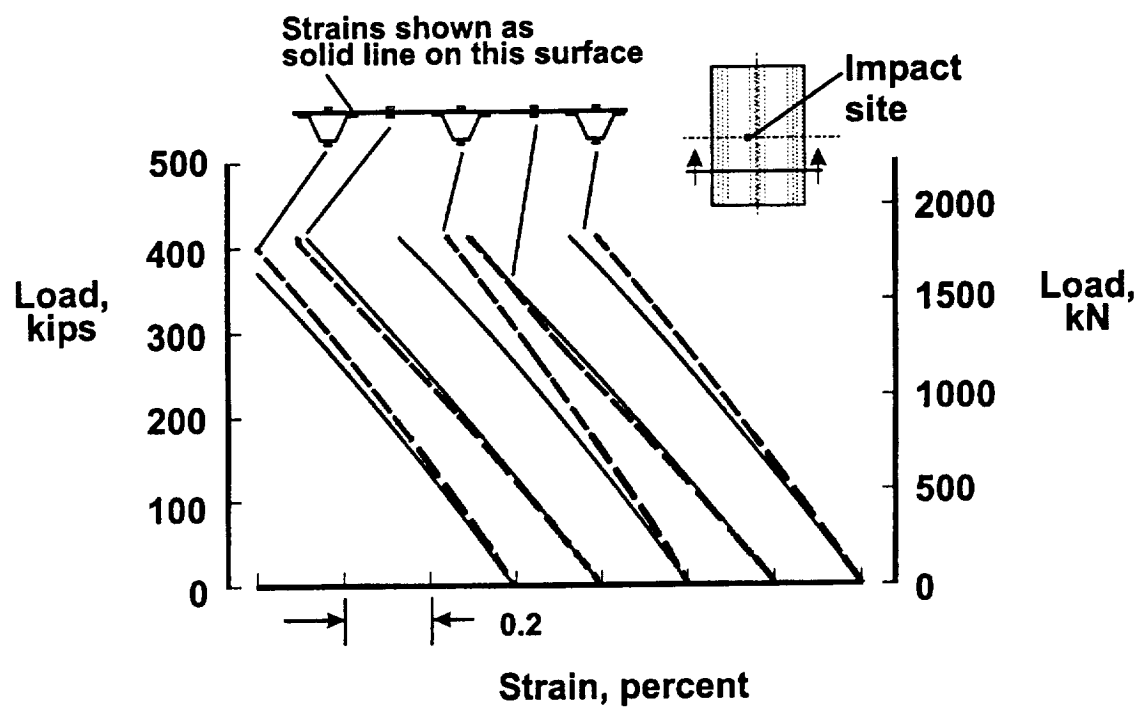
Figure 10f. – Load-strain response at cross-section located at quarter point of specimen HT1D1
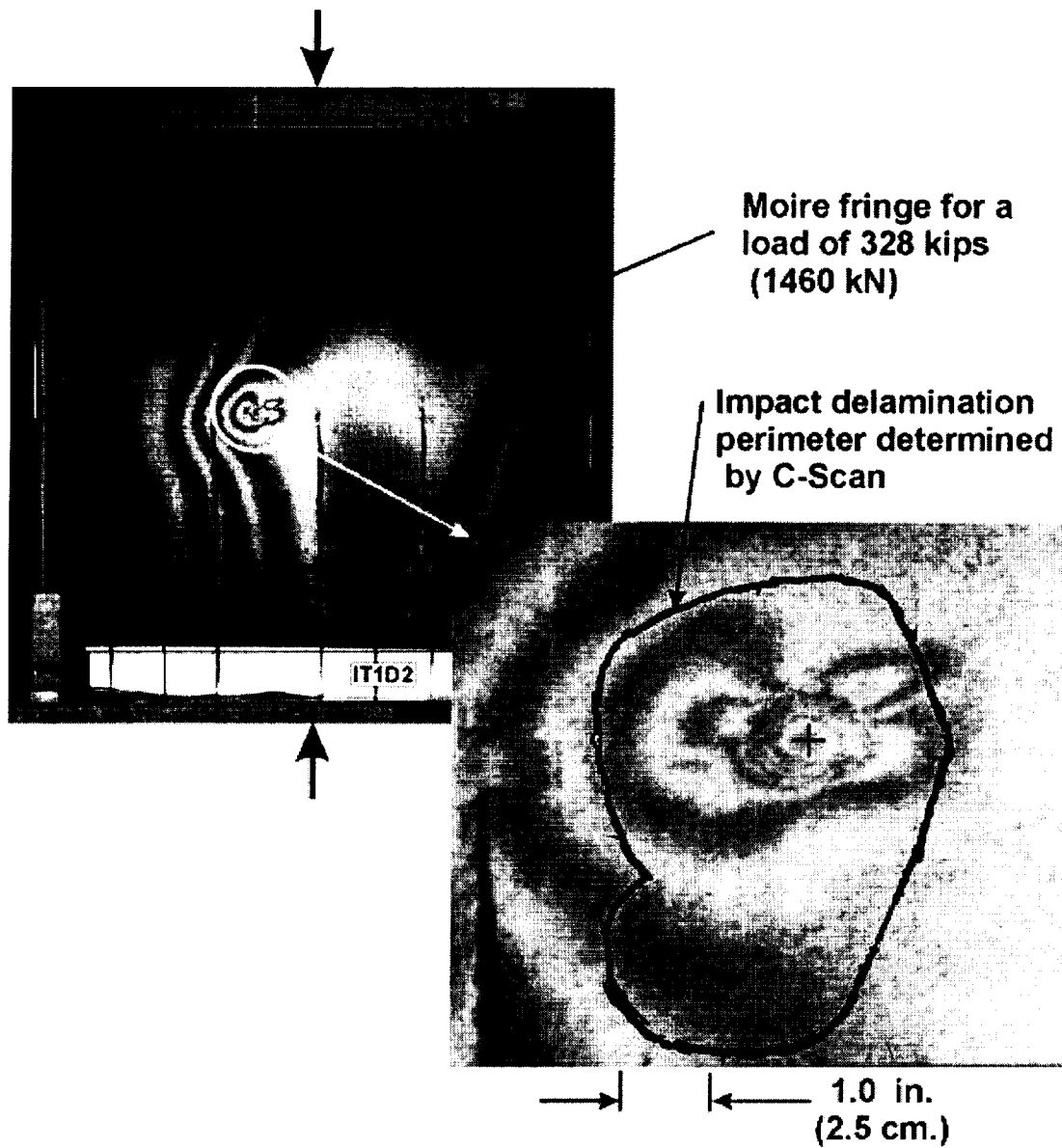
Figure 11. – Moiré fringe pattern and delamination perimeter of specimen IT1D2 at 328 kips
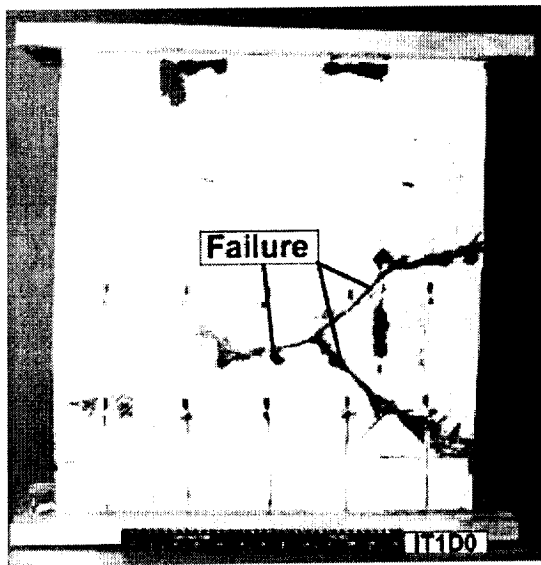
Figure 12a. – Failure location on skin side of Specimen IT1D0.
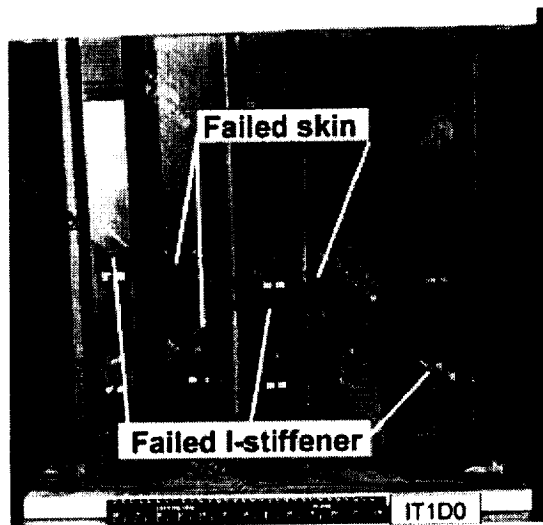
Figure 12b. – Failure location on stiffener side of Specimen IT1D0.
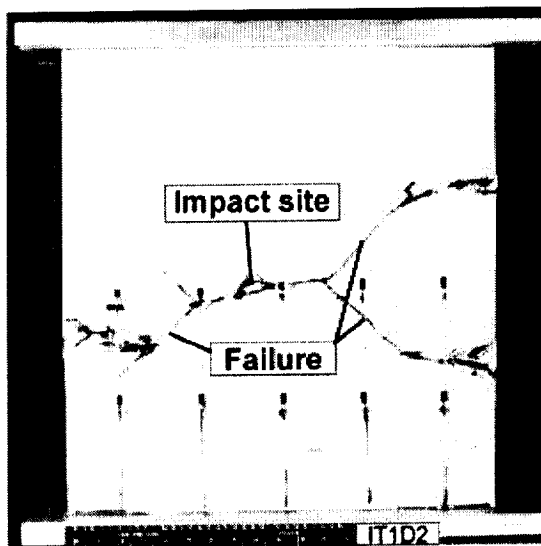
Figure 12c. – Failure location on skin side of Specimen IT1D2.
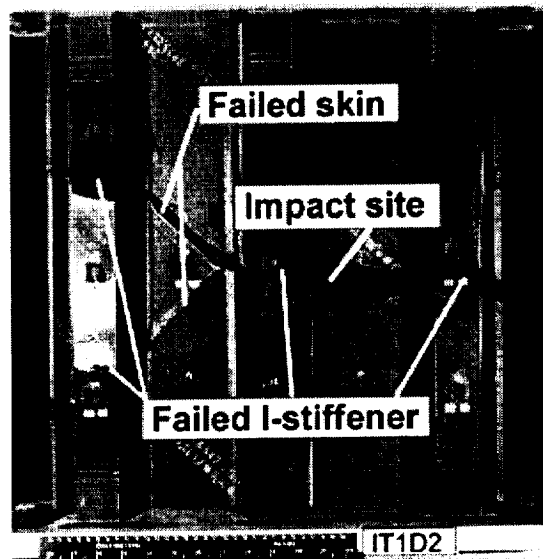
Figure 12d. – Failure location on stiffener side of Specimen IT1D2.
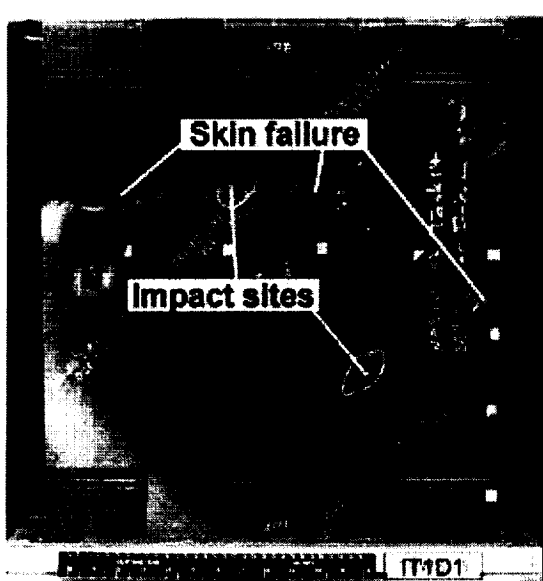
Figure 12e. – Failure location on skin side of Specimen IT1D1.
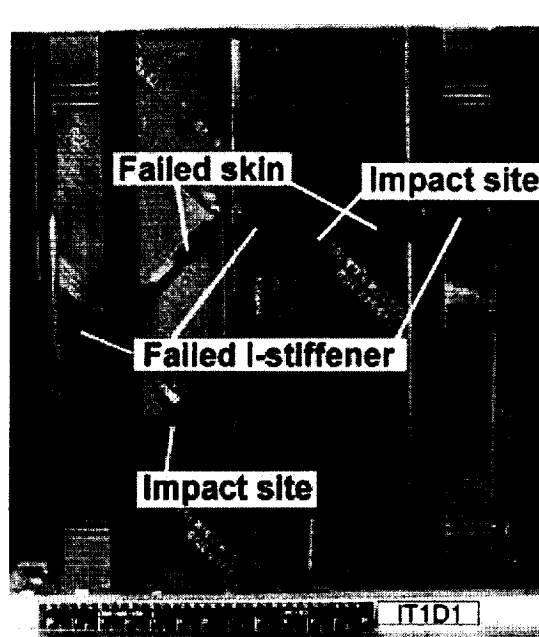
Figure 12f. – Failure location on stiffener side of Specimen IT1D1.
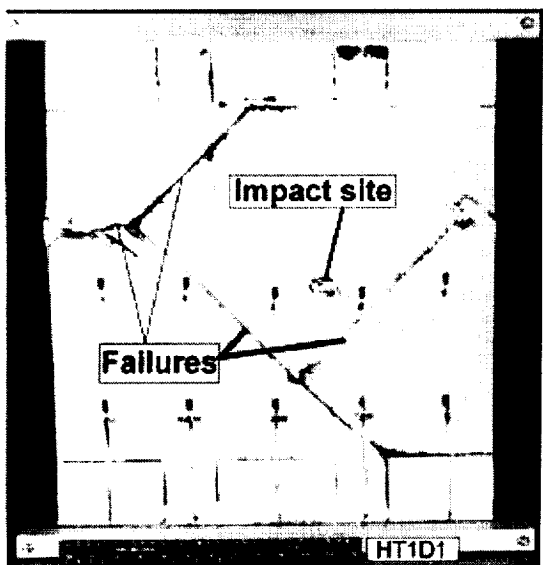
Figure 12g. – Failure location on skin side of Specimen HT1D1.
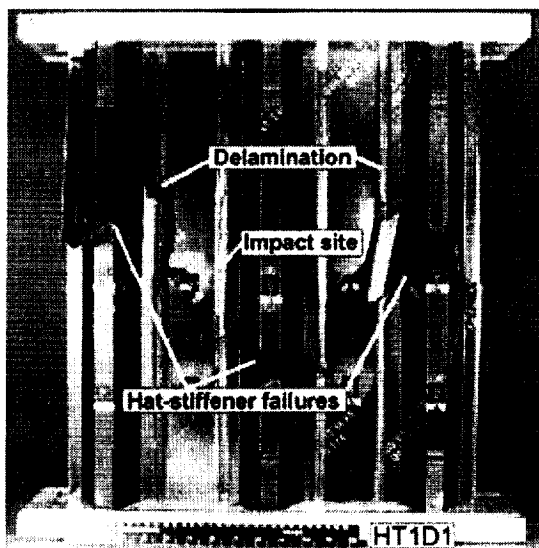
Figure 12h. – Failure location on stiffener side of Specimen HT1D1.

Nodes - 3086
Elements - 2976
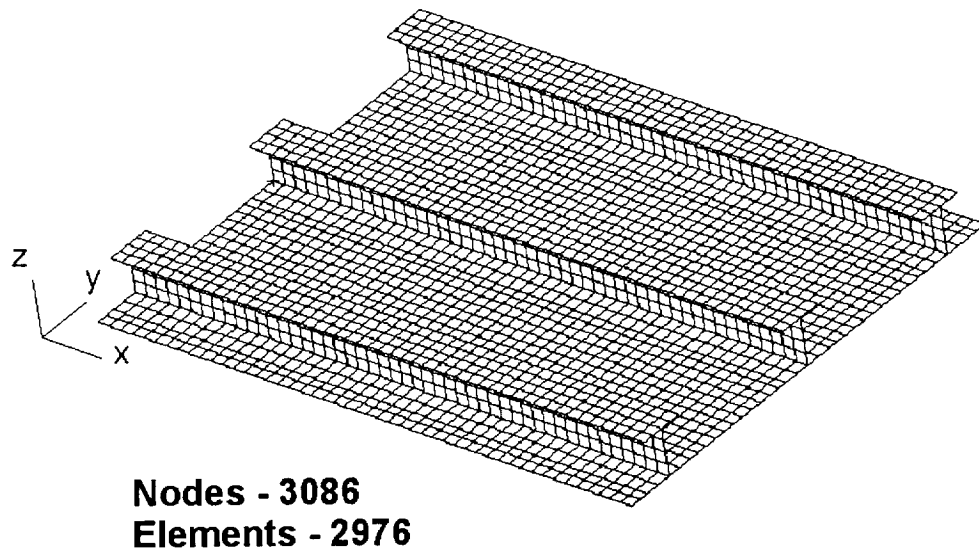
Figure 13. - Three stringer I-beam finite element mesh

Nodes - 3283
Elements - 3312
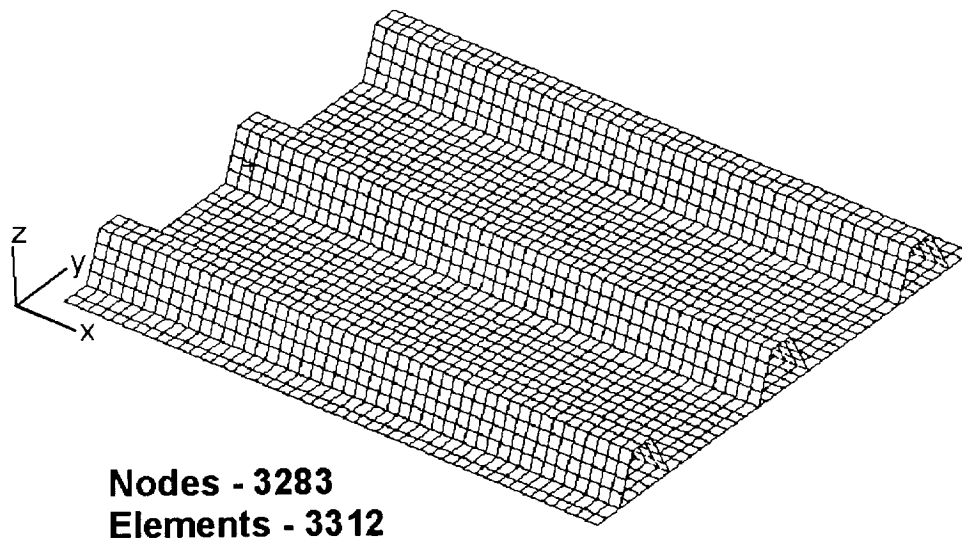
Figure 14. - Three stringer hat/plank-stiffened finite element mesh

P

x = 23.75 in.   u = δ_P
(60.3 cm.)

v = w = θ_y = 0

x = 23.25 in.   v = w = 0
(59.1 cm.)

x = 22.75 in.   v = w = 0
(57.8 cm.)

1.0 in.
(2.5 cm.)

23.75 in.
(60.3 cm.)

x

y

x = 1.0 in.   v = w = 0
(2.5 cm.)

x = 0.5 in.   v = w =0
(1.3 cm.)

x = 0.0   u = v = w = 0

θ_y = 0

Potted ends
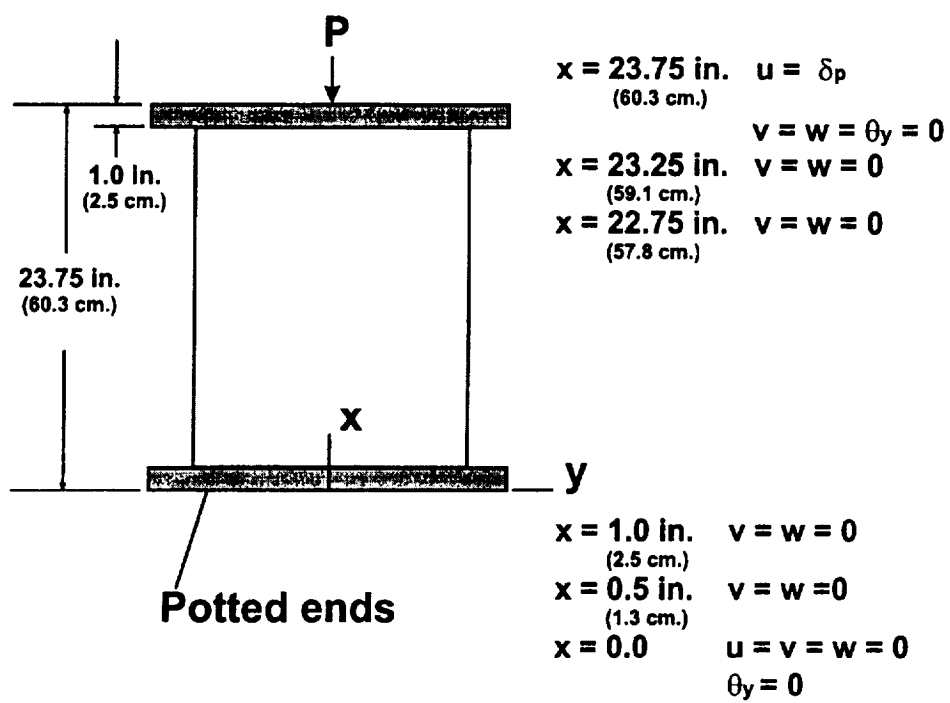
Figure 15. – Global finite element boundary conditions
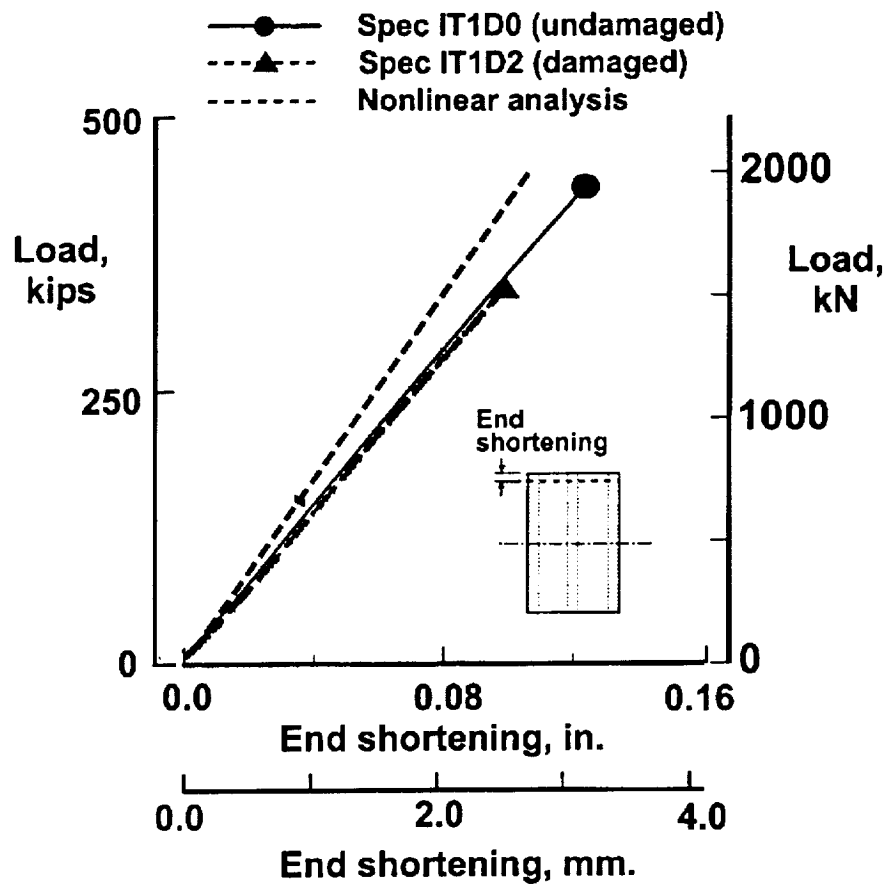
Figure 16a. – Comparison of end shortening of panels with the predicted.
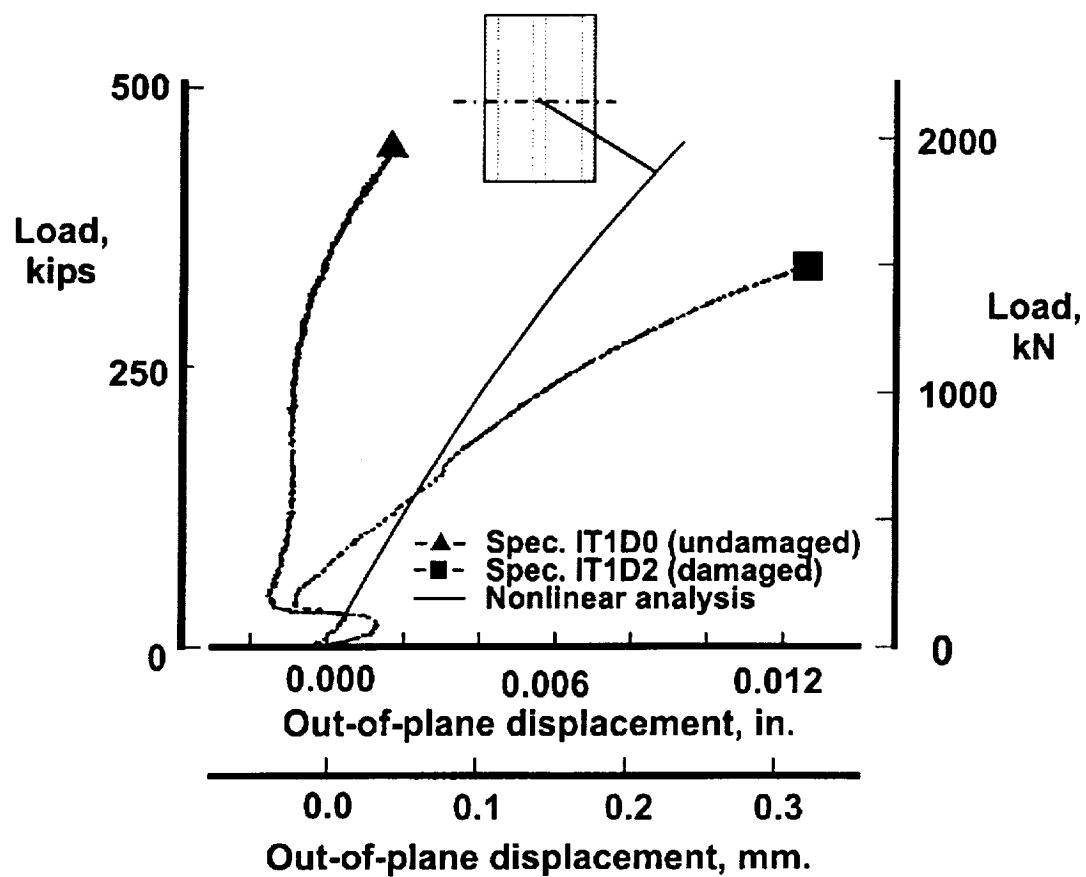
Figure 16b. – Comparison of the out-of-plane displacement.
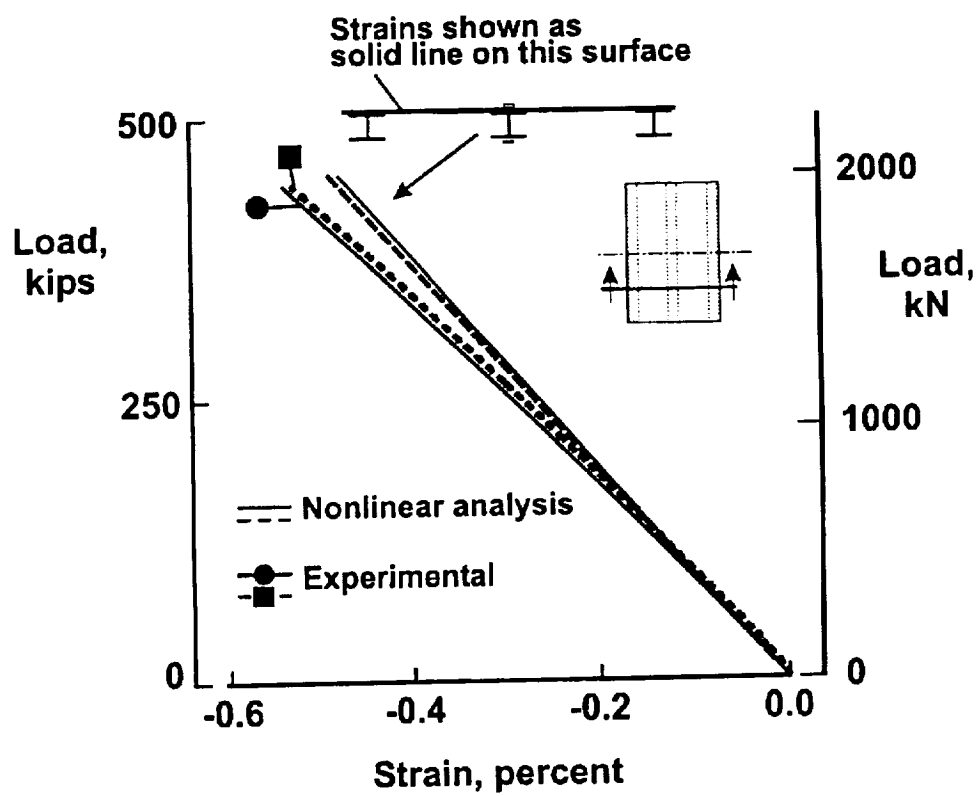
Figure 16c. – Strain results on centerline stiffener.
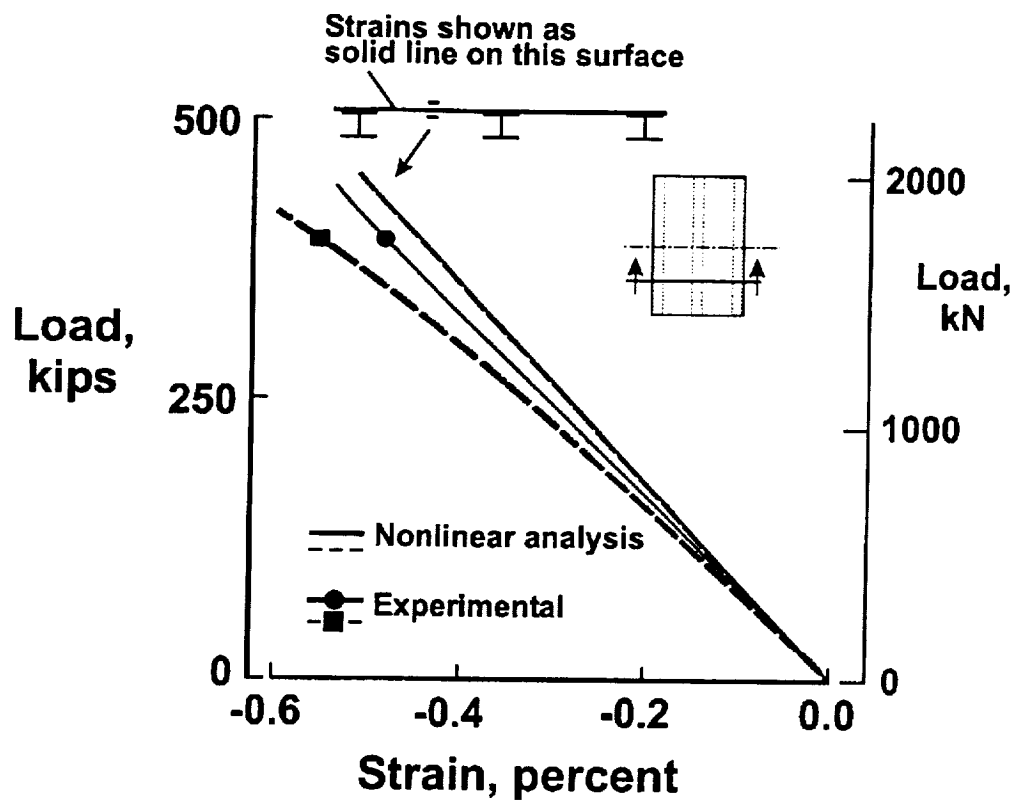
Figure 16d. – Strain results in the skin at the quarter point.
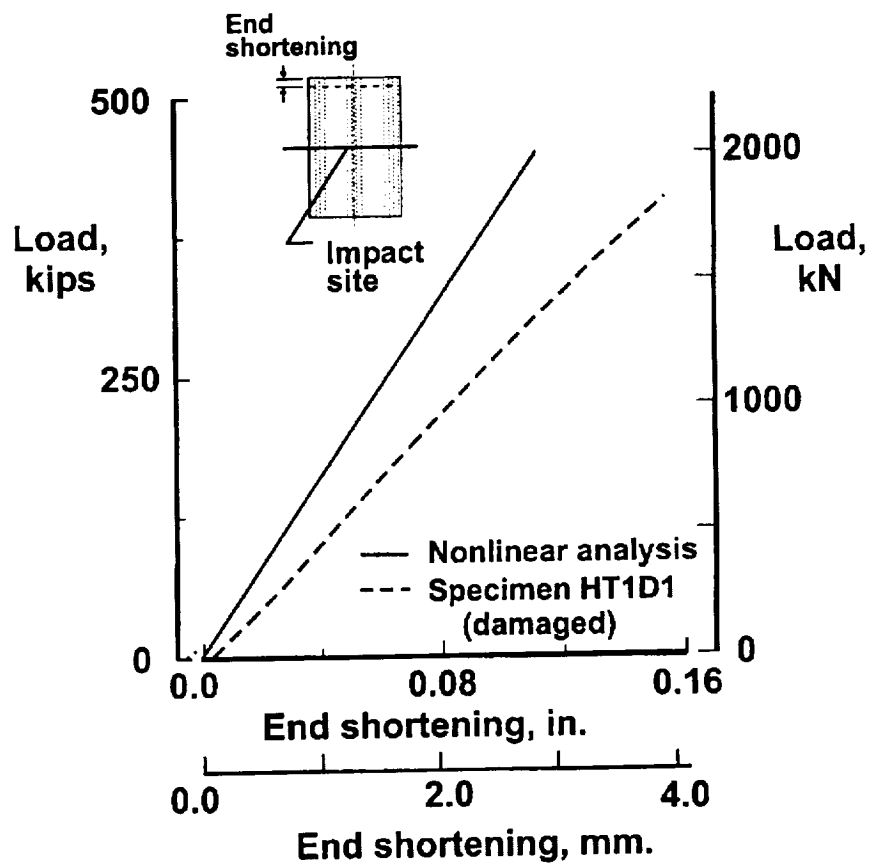
Figure 17. – Comparison of end shortening for hat-stiffened panels
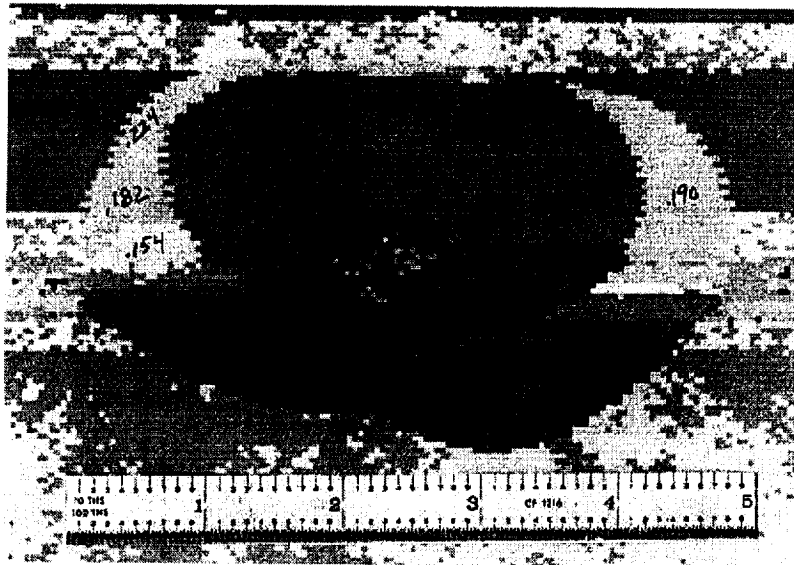
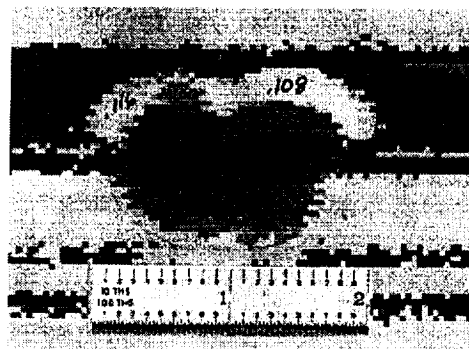Figure 18. - Typical TOF image for I-beam/plank/skin delamination

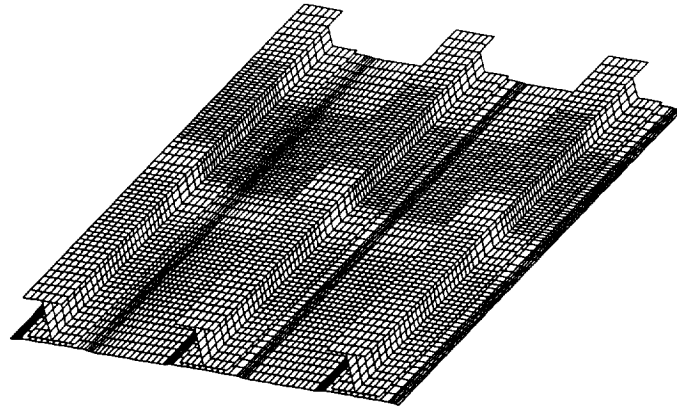Figure 19. - Typical TOF image for hard-skin/hat delamination
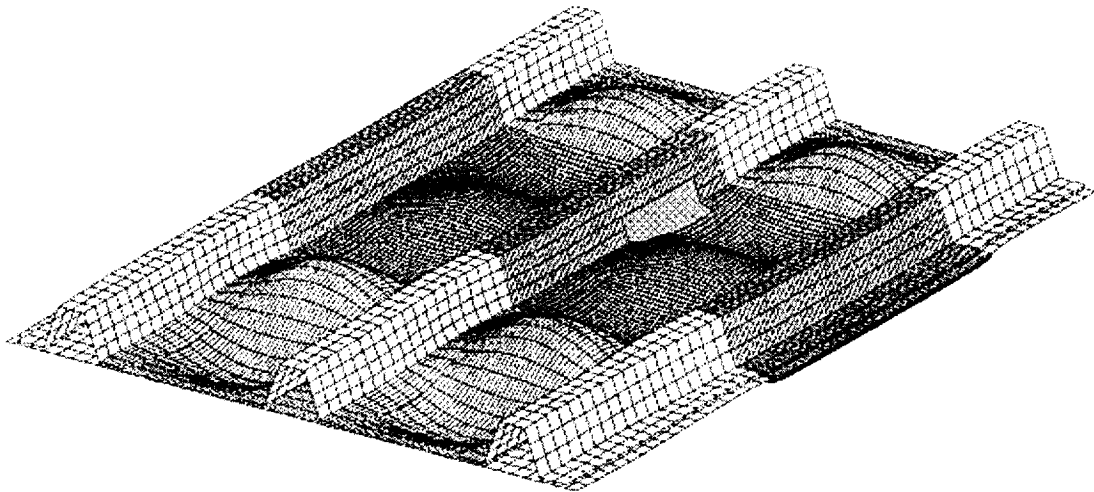
Figure 20. - Substructured I-beam panel FE mesh

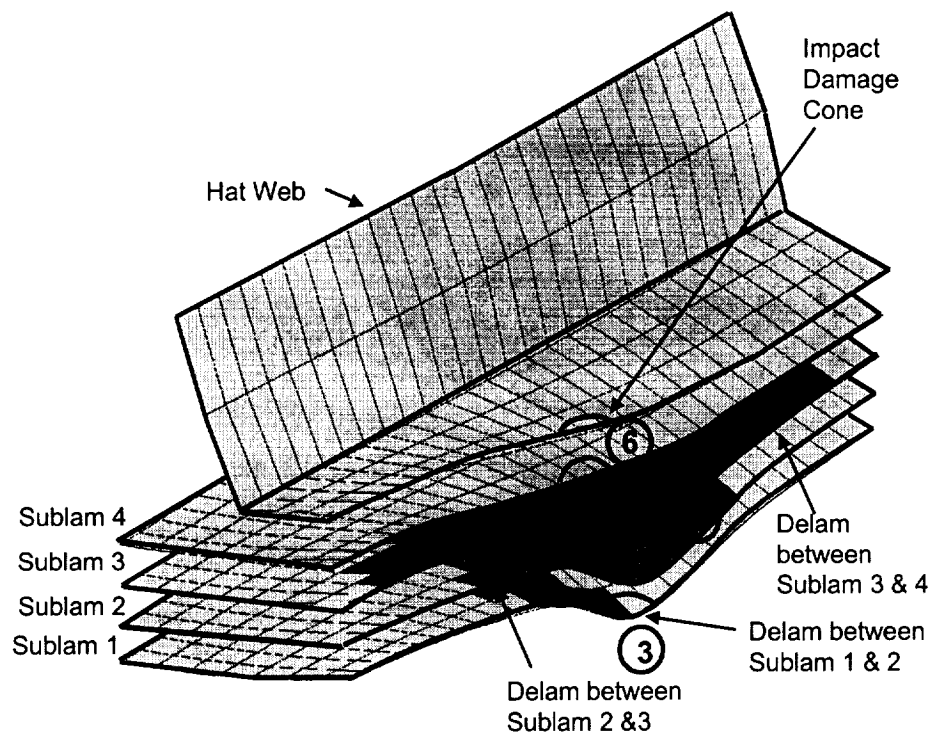Figure 21. - Substructured hat-stiffened panel FE mesh

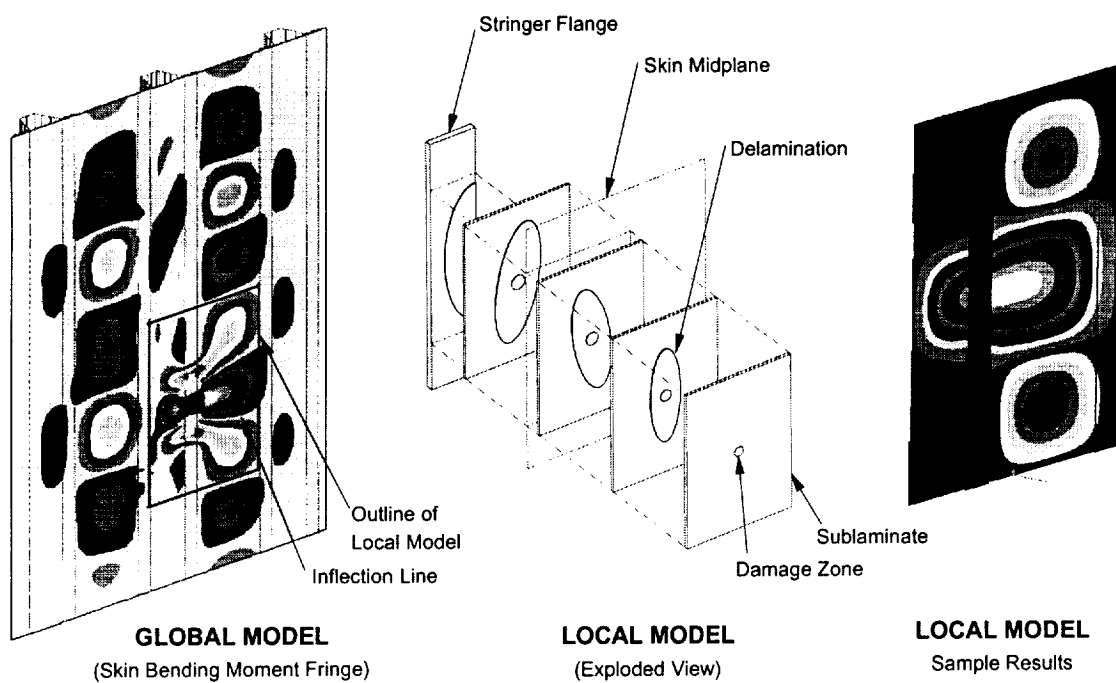Figure 22. - Exploded view of multi-layer substructure model (deformed mesh)

GLOBAL MODEL
(Skin Bending Moment Fringe)

LOCAL MODEL
(Exploded View)

LOCAL MODEL
Sample Results

Figure 23. - Illustration of global-local modeling approach

Initial Linear Response

Damage Induces Global Lateral Response

1st Sublaminate buckles and unloads

Loading rate to remaining Sublaminates Increase
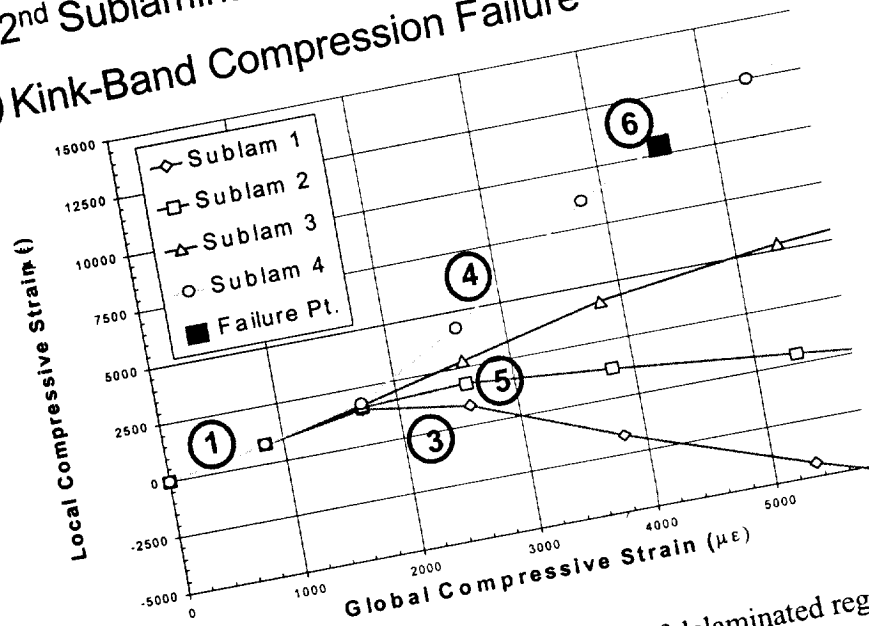
2nd Sublaminate buckles etc.

Kink-Band Compression Failure

Figure 24. - Nonlinear strain response of delaminated region